Construction of fish-scale tubular carbon nitride-based heterojunction with boosting charge separation in photocatalytic tetracycline degradation and H$_2$O$_2$ production

Qinghua Liang [a,1], Xiaojuan Liu [b,1], Binbin Shao [a,1], Lin Tang [a,1], Zhifeng Liu [a,*], Wei Zhang [b], Shanxi Gong [c], Yang Liu [a], Qingyun He [a], Ting Wu [a], Yuan Pan [a], Shehua Tong [a]

[a] College of Environmental Science and Engineering, Hunan University and Key Laboratory of Environmental Biology and Pollution Control (Hunan University), Ministry of Education, Changsha 410082, PR China
[b] The First Affiliated Hospital of Hunan University of Chinese Medicine, Changsha 410007, PR China
[c] School of Chemistry and Chemical Engineering, Guangxi University, Nanning 530004, PR China

ARTICLE INFO

ABSTRACT

A fish-scale tubular carbon nitride (FTCN$_{so}$) and its heterojunction ZnIn$_2$S$_4$/FTCN$_{so}$ were constructed to enhance the ability of photocatalytic tetracycline degradation and H$_2$O$_2$ production under visible light. The photocatalysts were analyzed through a variety of techniques. Firstly, the surface of FTCN$_{so}$ was composed of fish-scale nanoplatelets with abundant structural defects by SEM. Secondly, the results of UV–vis and theoretical calculation proved the improvement of visible light absorption performance of ZnIn$_2$S$_4$/FTCN$_{so}$. Thirdly, the electrochemical tests confirmed the ZnIn$_2$S$_4$/FTCN$_{so}$ effectively inhibited the recombination of photogenerated e$^-$-h$^+$ pairs. Meanwhile, the electronic-structural properties and photocatalytic mechanism were systematically and deeply studied by combining UV–vis, XPS valence band, theoretical calculations and capture experiments of active species in different pH solution. ZnIn$_2$S$_4$/FTCN$_{so}$ exhibited excellent performance in photocatalytic tetracycline degradation and H$_2$O$_2$ production under visible light due to the special structure and the existence of heterojunction. This work provides guidance for the development and design of new multifunctional carbon nitride-based materials.

1. Introduction

With the rapid economic development, environmental contamination and energy shortage have become urgent issues that need to be resolved nowadays [1–4]. As one of the broad-spectrum antibacterial agent, tetracycline has been widely used in the field of medicine [5–8]. Since tetracycline is ubiquitous in the environment, it will seriously pollute the environment and threaten the safety of human life. In terms of energy, H$_2$O$_2$ has attracted much attention not only because it is an energy source for fuel cells, but H$_2$O$_2$ is also a clean general-purpose oxidant for disinfection and environmental remediation [9–11]. However, some common methods of producing H$_2$O$_2$, such as anthraquinone method and electrocatalytic oxygen reduction method, are often complicated in the operate process and high cost, which are not conducive to their use in industrial. Photocatalysis technology using clean solar energy is considered to be an effective strategy to solve the current environmental and energy crisis [12–15]. Traditional semiconductor photocatalysts, such as TiO$_2$ [13], BiOCl [16], and ZnO [17], usually have weak visible light (VSL) absorption and rapid electron-hole recombination rate, which inhibits their photocatalytic performance and restricts comprehensive application. In order to solve these problems, a variety of techniques for controlling defects and structural engineering are used, including element doping [18], morphology controlling [19], co-catalyst introducing [20] and heterojunction constructing [21].

Non-metallic carbon nitride (CN) with a suitable band gap structure (2.7 eV) has received extensive attention, due to low cost, suitable band gap, easy preparation and good stability [22–24]. However, the original

---

CN has a low specific surface area, weak VSL absorption and fast electron-hole recombination rate, a lot of research on defect and structural engineering has been carried out [25–27]. Self-assembly technology based on the interaction between small molecules is usually used to prepare materials with regular structures. The construction of CN with specific structures through self-assembly methods has received more attention, such as melamine structural analogs, small molecules rich in functional groups, carbon-based macromolecules with large π bonds, and thermally unstable substances, which can occur self-assembly with melamine into multiple dimensions of CN-based materials [28]. Particularly, the tubular structure of 1D CN can control the transfer of electrons and holes and inhibit their recombination, and enhance the light absorption capacity, thereby contributing to the improvement of photocatalytic performance [19,29,30].

In our previous work, we studied the self-assembly behavior of melamine and trithiocyanuric acid in ethanol/water solution and obtained a tubular CN-based photocatalyst. However, the self-assembly behavior was insufficient due to insoluble melamine, resulting in insufficient self-assembly between small molecules. Meanwhile, the prepared 1D CN had a small pore structure and is not suitable as a carrier for composite materials. Interestingly, some papers reported the influence of solvents on structural reformation [28]. For example, Jun et al. studied the self-assembly behavior of melamine and cyanuric acid in DMSO solvent, and the results showed that the obtained spherical structure was not the traditional tubular structure [31]. Therefore, it is necessary to expand the scope of research on the self-assembly behavior of melamine under sufficient dissolution. Meanwhile, it is interesting thing if defects and abundant pores are generated through self-assembly, which is conducive to the construction of good photocatalysts carrier.

It should be emphasized that 1D CN has a more stable framework structure than other carbon nitrides, making it suitable as a photocatalyst carrier. Wang et al. used 1D CN as a carrier and modified it with black phosphorus quantum dots [29]. The obtained heterojunction photocatalyst has excellent performance for oxytetracycline hydrochloride degradation and hexavalent chromium reduction. Unfortunately, there are few studies on the construction of high-performance composite heterostructures with 1D CN as carriers [32–34]. Therefore, it is urgent to develop high-performance photocatalyst composite materials based on the 1D CN carrier. For the construction of photocatalytic composite materials, the choice of components is extremely important. Generally, the band gap structure of the material, the electron transfer mechanism, the interaction force between the materials, and the tightness of the heterojunction are considered. The sulfide metal $ZnIn_2S_4$ is an ideal photocatalyst due to its suitable band gap (2.2–2.6 eV), adjustable morphology and strong VSL absorption capacity [35–37]. In addition, according to the results of some literatures, $ZnIn_2S_4$ can be tightly combined with CN, which may be due to the existence of strong cation-π interaction, leading to enhanced in photocatalytic activity [38–41]. Therefore, several articles using $ZnIn_2S_4$ and CN to construct heterostructures have been reported [42–44]. However, the current research is mainly based on 2D materials, and the $ZnIn_2S_4$ heterojunction based on 1D CN has not been reported. Interestingly, photocatalyst materials of different dimensions usually show various properties. Meanwhile, according to some research results, it can be found that $ZnIn_2S_4$ can be well combined with 1D materials to build a tight heterojunction interface [38,39]. Zhang et al. prepared hierarchical $Co_9S_8/ZnIn_2S_4$ tubular heterostructures using a low-temperature hydrothermal method. This material has excellent solar energy conversion efficiency due to the perfect heterojunction structure [45]. Therefore, based on a large number of research results, we speculate that $ZnIn_2S_4$ can easily construct a high-performance heterojunction photocatalyst with 1D CN. Under the premise of matching the valence band and the conduction band, it is a good choice to combine the wide band gap of 1D CN and the strong light absorption of $ZnIn_2S_4$ to construct a composite heterojunction photocatalyst. The structure of the heterostructure can not only overcome the shortcomings of 1D CN and $ZnIn_2S_4$

semiconductors, but also combine the advantages both of them to obtain high-performance photocatalyst.

In this study, firstly, the morphology of CN was adjusted to improve its band gap structure and enhance photocatalytic performance. Melamine and volatile trithiocyanuric acid were dissolved in an organic solvent, and then they were completely self-assembled and calcined to obtain a novel type of porous fish-scale tubular CN ($FTCN_{so}$). The $FTCN_{so}$ had a small nanostructure, a large number of pores and structural defects, and obvious boundaries, which facilitated the transfer of charge and photoelectrons. In addition, the structure of fish scales helps to improve the crystallinity of the material. Due to its rich pore structure and excellent photocatalytic performance, $FTCN_{so}$ was considered a potential photocatalytic carrier. Therefore, the $FTCN_{so}$ was used as a carrier to construct a heterojunction complex to improve charge transfer performance and photocatalytic activity, and the $ZnIn_2S_4$ was grown in situ on the surface of the $FTCN_{so}$. This novel $ZnIn_2S_4/FTCN_{so}$ heterostructure possess abundant pores, structural defects and active sites, remarkable electron-hole separation and transfer ability, sufficient photocatalytic kinetic energy and strong VSL absorption ability. Accordingly, the heterojunction composite exhibited excellent photocatalytic degradation of tetracycline and H_2O_2 production. Moreover, the heterojunction composite material had been fully explored and the mechanism analyzed through a series of systematic experiments, characterization techniques and theoretical calculations. This work proves that the fish-scale tubular $ZnIn_2S_4/FTCN_{so}$ heterostructure constructed by simple self-assembly technology has strong VSL photocatalytic performance and has excellent application potential in the environmental and energy field.

2. Experimental

2.1. Chemicals and materials

All reagents used in this experiment are of analytical grade. Melamine (Sinopharm Chemical Reagent Co., Ltd, 99%), trithiocyanuric acid (9 ding Biotechnology Co., Ltd, 95%), tetracycline hydrochloride (TCH) (Bomei biological technology Co., Ltd, 98%), dimethyl sulfoxide (DMSO) (Tianjin Fuyu Fine Chemical Co. Ltd, 98%) were used as received. The ultra-pure water (18.25 MΩ cm^{-1}) was used throughout the experiment.

2.2. Construction of ZnIn$_2$S$_4$/FTCN$_{so}$

Preparation of FTCN$_{so}$. The fish-scale tubular $FTCN_{so}$ with abundant structural defects was carried out by self-assembly method. Generally, the solubility of melamine and trithiocyanuric acid in water is poor, which limits the realization of perfect self-assembly between them and affects the photocatalytic performance of the material. Hence, DMSO was used as a solvent to dissolve melamine and trithiocyanuric acid. Firstly, 1.26 g of melamine was dissolved in 30 mL of DMSO, while 1.77 g of trithiocyanuric acid was dissolved in 20 mL of DMSO, and then the trithiocyanuric acid solution was added dropwise to the melamine solution under stirring. After stirring for 2 h, 100 mL of ultra-pure water was added to the above solution to obtain a yellow precipitate. The precipitate was filtered, washed, dried, ground and then calcined at 550 °C (2.3 °C min^{-1}) under N_2 atmosphere for 4 h in a tube furnace [46]. After natural cooling and grinding, the sample was obtained and recorded as $FTCN_{so}$. As for comparison, the prepared photocatalyst under insolubility conditions was named TCN_{iso} [47].

Preparation of ZnIn$_2$S$_4$/FTCN$_{so}$. 235 mg of $FTCN_{so}$ and 80 mL of H_2O were added to a polytetrafluoroethylene liner, ultrasonicated for 30 min to disperse, and then a certain amount of $ZnCl_2$, $lnCl_3$ and CH_3COSH were sequentially added every 5 min. After stirring for 30 min, it was placed in an autoclave and reacted in an oven at 180 °C for 10 h [35,48]. Then, it was fully washed with ethanol and deionized water and dried. The final product was named as x% $ZnIn_2S_4/FTCN_{so}$, where × was the

proportion of $ZnIn_2S_4$ in the composite. The detailed preparation flow chart is shown in Scheme 1.

2.3. Structural characterization methods

The morphology and microstructure of $ZnIn_2S_4/FTCN_{so}$ heterojunction were revealed by SEM (FEI Quanta-F250) and TEM (FEI Tecnai-G2 F20). The crystal phase structure was obtained using a XRD (Bruker AXS D8, Cu-Ka radiation). The surface element composition and element environment were surveyed by XPS (PHI 5300 ESEA, Al Kα radiation). The specific surface area (Brunauer − Emmett − Teller) and pore distribution were performed at − 196 °C using an analyzer (Quantachrome Quadrasorb SI). The UV–vis diffuse-reflectance spectra were obtained by a Varian Cary 300 spectrometer (Shimadzu UV-2600) using $BaSO_4$ as the standard. The photo-luminescence (PL) spectra, electrochemical impedance spectroscopy (EIS) and photocurrent were investigated by an electrochemical analyzer (CHI 660C) under VSL illumination. The ESR signals were measured on a spectrometer (Bruker, Germany) under VSL illumination. The total organic carbon (TOC) dates were obtained by a Shimadzu TOC-LCPH analyzer.

2.4. Measurement of photocatalytic activity

Photocatalytic degradation of TCH solution (10 mg L^{-1}) was carried out to evaluate the photocatalytic activity of as-prepared samples. Typically, 25 mg of as-prepared samples were added to 50 mL of TCH solution. Firstly, a dark reaction was performed, and the above mixture was stirred in a dark environment for 30 min for sufficient adsorption. Then, photocatalytic degradation experiments were conducted under VSL irradiation (300 W Xe lamp, λ > 420 nm, 100 mW cm^{-2}). During the degradation process, 1.0 mL degradation solution was withdrawn every 5 min, and then the concentration was measured in a UV–vis spectrophotometer (273 nm). The content of H_2O_2 was determined by the coloration method of potassium iodide (KI) and potassium hydrogen phthalate ($C_8H_5KO_4$). Typically, 50 mg of as-prepared samples were added to 100 mL of water solution. Firstly, the mixed solution was sonicated for 10 min to make it fully mixed, and then oxygen was introduced for 30 min under dark conditions with stirring. Finally, the H_2O_2 production experiment was conducted under VSL irradiation.

After the reaction is complete, add 1 mL of 0.1 mol L^{-1} $C_8H_5KO_4$ solution and 0.4 mol L^{-1} KI solution respectively, and keep them for 30 min to fully react ($H_2O_2 + 3I^- + 2H^+ \rightarrow I_3^- + 2H_2O$) [49]. Because I_3^- has a strong absorption peak at around 350 nm, the content of H_2O_2 was determined by the UV–Vis spectrometer.

2.5. Theoretical calculation method

Density functional theory (DFT) was used to study and analyze the prepared samples by the software of Materials Studio 8.0 [50]. The calculations based on DFT were constructed based on Perdew − Burke − Ernzerhof (PBE) in the generalized gradient approximation (GGA). The theoretical model of $FTCN_{so}$ used in this research is based on the melon structure [51,52]. Since our research focuses on the physical and chemical properties of materials, the data calculated under the same calculation parameters can be compared and explain the changes in properties.

The geometric configuration of the material was mainly optimized, the electronic structure and energy band properties of the material are analyzed, and the charge transfer at the interface of the heterojunction was explored through theoretical calculations. The energy cut-off of plane wave extension for several models is set to 435.4 eV. The k-point mesh of $2 \times 2 \times 1$ was used to geometry optimization and energy-related calculations. The distance of the vacuum layer was set to 15 Å to avoid the interference interaction between adjacent interfaces. The pseudo-potential was OTFG ultrasoft, and relativistic treatment was based on Koelling-Hamon. In addition, in order to ensure the accuracy of the calculation, the maximum step size, force, energy change and stress were set to 0.001 Å, 0.03 eV/Å, 1.0×10^{-5} eV/atom and 0.005 GPa, respectively. The optimal geometric configuration and lattice parameters of prepared samples were shown in Fig. 5A-C and Table 2, respectively.

3. Results and discussion

3.1. Characterization of samples

3.1.1. Morphology, crystal and chemical states analysis

The morphology and structure of the material were analyzed by SEM
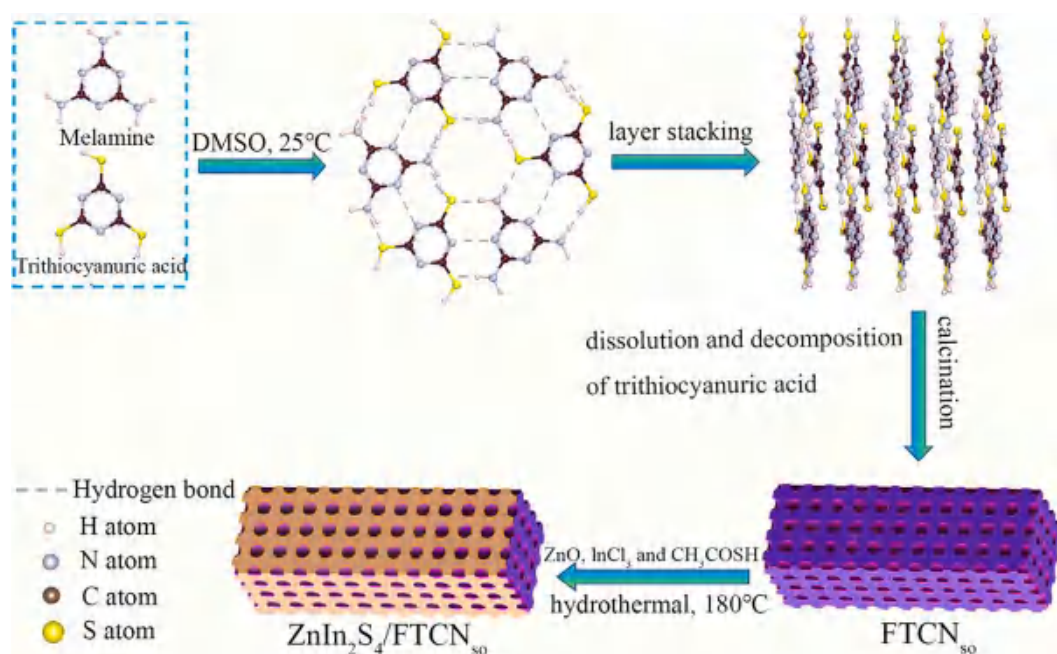
Scheme 1. Schematic diagram of the preparation process of a novel fish-scale porous tubular carbon nitride heterojunction compound $ZnIn_2S_4/FTCN_{so}$.

and TEM. The original carbon nitride has a bulk structure (Fig. 1A). The FTCN$_{so}$ precursor showed a smooth tubular structure before calcination (Fig. S1A), which indicated that trithiocyanuric acid and melamine could fully self-assemble in a dissolved environment. As shown in Scheme 1, a regular polygonal structure was formed through the hydrogen bond interaction between melamine and trithiocyanuric acid firstly, and then polygonal structures were close to each other due to the π-π stacking interaction, resulting in the formation of a tubular structure [19,47,53]. The surface of the FTCN$_{so}$ obtained after calcination was rough, and the surface was covered by a large number of nanopores (Fig. 1C and 1D). The existence of a host of pores causes the material has abundant structural defects, which will affect the performance of the material [27,54]. It was worth emphasizing that the novel tubular structure of FTCN$_{so}$ was composed of many fish scales of about 100 nm (Fig. 1D). The unique fish scale structure endowed the space transfer effect of electrons, and the electrons were selectively transferred to the edge of the fish scale, which was beneficial to improve the separation efficiency of charges [55].

Although several papers had reported on fish scale CN [55–57], the fish scale CN obtained by direct calcination had not been reported. In

order to study the change process of the material, we studied the change of the material surface under different temperatures and calcination times, and the results were shown in Fig. S1A-F. When the calcination temperature was 200 °C, a small amount of voids appeared on the surface of the material, which was attributed to the volatilization of crystal water inside the material. When the temperature further increased to 450 °C, the surface structure of the material began to partially decompose. As the temperature further increased to 550 °C, scale-like structures began to appear on the surface of the material after calcination for 1 h, and the reaction was basically completed after calcination for 2 h. According to the change process in Fig. S1A-F, we speculated that as the temperature gradually reached the reaction temperature, a large number of void structures began to appear, which was caused by the decomposition of the substance and the H$_2$S and NH$_3$ gases produced during the reaction. As the temperature further increased, porous structures and fish-scale structures gradually formed, which might be caused by the edge effect of self-assembled aggregates. Due to the edge effect, the force field at a certain distance was weak, and supramolecular aggregates were easy to move and break, which resulted in the formation of scale-like structures. However, the surface of TCN$_{iso}$ obtained
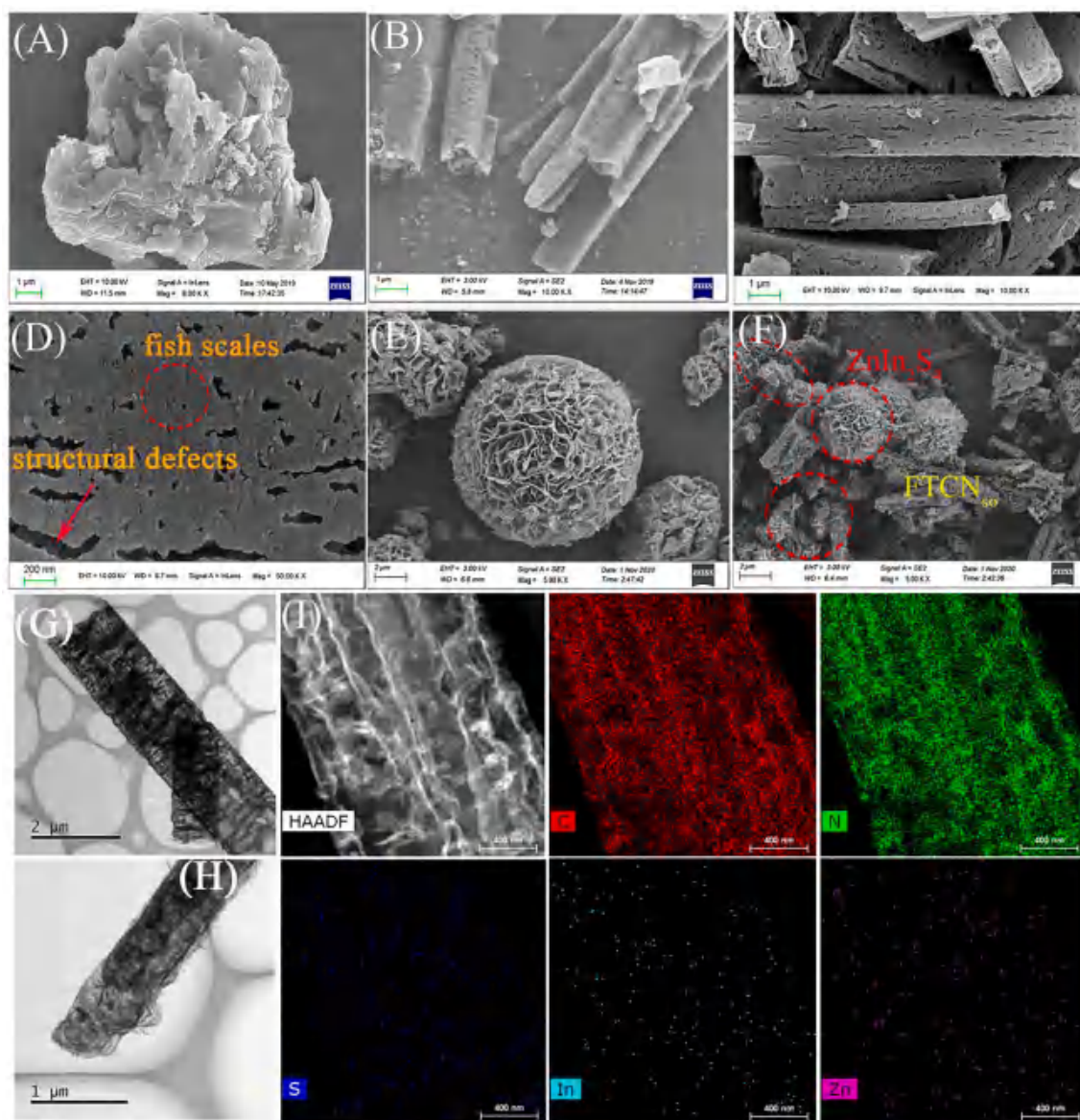

Fig. 1. SEM images of bulk CN (A), TCN$_{iso}$ (B), FTCN$_{so}$ (C) and (D), ZnIn$_2$S$_4$ (E), and ZnIn$_2$S$_4$/FTCN$_{so}$ (F); TEM images of FTCN$_{so}$ (G) and ZnIn$_2$S$_4$/FTCN$_{so}$ (H); HRTEM images and elemental mapping images of ZnIn$_2$S$_4$/FTCN$_{so}$ (I).

under insufficient dissolution conditions was relatively smooth and lacks pore structure (Fig. 1B), which could not serve as a good carrier and construct composite materials. As for another semiconductor, $ZnIn_2S_4$ had a spherical flower-like structure with abundant folds (Fig. 1E), and its surface was mainly composed of (220) and (311) crystal planes (Fig. S1G) [43]. The $ZnIn_2S_4/FTCN_{so}$ obtained after in-situ growth and compounding retained the tubular skeleton structure of $FTCN_{so}$, and the surface had some changes due to the covering of $ZnIn_2S_4$ (Fig. 1F and 1H). According to the different stages of crystal growth, the existence of $ZnIn_2S_4$ on the wall of $FTCN_{so}$ was divided into two types. One was a microspherical flower-like structure, and the other was a petal-like package on the wall of $FTCN_{so}$ (Fig. 1F, 1H and S1H). Although the morphology of the composite material was somewhat different from that reported in the literature [45,58], we could see that the particle size of the composited $ZnIn_2S_4$ had been significantly reduced, which was conducive to contact with the fish-scale tubular $FTCN_{so}$. In addition, the element scanning mapping of the tubular composite structure showed that $ZnIn_2S_4$ was evenly dispersed around $FTCN_{so}$, which indicated that the composite material had the characteristics of uniform distribution and compactness. In summary, the successful construction of composite materials with abundant structural defects can be confirmed.

The XRD patterns of the prepared sample were shown in Fig. 2A. As for CN, TCN_{iso}, $FTCN_{so}$ and $ZnIn_2S_4/FTCN_{so}$, there were four obvious diffraction peaks in total. In detail, the peak at 13.2° (210))$_{orthorhombic}$ corresponded to the in-plane structure stacking of triazine units, and the other peak at 27.4° (002) corresponded to the interlayer stacking of aromatic units [59,60]. It was worth emphasizing that the $FTCN_{so}$ prepared by self-assembly with fully dissolved retained the crystal structure of CN, while the crystal structure of TCN_{iso} prepared by self-assembly with insufficient dissolution was seriously damaged, which was attributed to the more complete and sufficient self-assembly behavior under sufficient dissolution. In addition, the fish scale structure was beneficial to improve the crystallinity, which was consistent with previous reports [55]. Importantly, the orderly structure inside is beneficial to enhance photocatalytic activity. The XRD spectra of $ZnIn_2S_4/FTCN_{so}$ heterojunction appeared with the increase of $ZnIn_2S_4$ content. On the one hand, the diffraction peaks (13.2°, 27.4°) of CN gradually became weaker and disappear. On the other hand, the diffraction peaks at 21.6° (006), 27.7° (102), and 47.2° (110) gradually increased [36]. In addition, the results of XRD confirmed the successful preparation of composite heterojunctions.

The pore structure and specific surface area of the prepared material were studied by N_2 adsorption–desorption (Fig. 2B). All samples were typical type III isotherm, indicating all samples had mesoporous structure. Then, the BJH adsorption method and the BET method were used to analyze the pore size distribution and specific surface area, respectively. The results were shown in Fig. 2B and Table 1. CN and $ZnIn_2S_4$

Table 1
The pore structure parameters of CN, $FTCN_{so}$, $ZnIn_2S_4$ and $ZnIn_2S_4/FTCN_{so}$.

Sample	BET surface area (m^2/g)	Pore volume (cm^3/g)	Average pore size (nm)
CN	23.33	0.25	31.86
$FTCN_{so}$	89.87	0.54	24.11
$ZnIn_2S_4$	12.45	0.10	32.78
$ZnIn_2S_4/$ $FTCN_{so}$	69.15	0.47	27.04

Table 2
Lattice parameters of the $FTCN_{so}$, $ZnIn_2S_4$ and $ZnIn_2S_4/FTCN_{so}$.

Samples	Lattice types	Lengths (Å)			Angles (°)		
		a	b	c	α	β	γ
$FTCN_{so}$	3D triclinic	16.73	12.71	15	90.00	90.00	90
$ZnIn_2S_4$	3D triclinic	20.23	11.90	24.46	90.00	90.00	90
$ZnIn_2S_4/$ $FTCN_{so}$	3D triclinic	18.48	12.30	32.05	90.00	90.00	90

had few pores, while $FTCN_{so}$ and $ZnIn_2S_4/FTCN_{so}$ had a large number of mesopores about 30 nm. Furthermore, $FTCN_{so}$ had a larger specific surface area than CN and $ZnIn_2S_4$, which was related to the abundant pores. This also made $ZnIn_2S_4/FTCN_{so}$ had a large specific surface area due to the presence of porous $FTCN_{so}$. The rich pore structure and large specific surface area provide more catalytically active sites and promote the adsorption of pollutants, which is conducive to the improvement of photocatalytic activity.

In order to understand the surface chemical structure properties of the material, an XPS tester was used for evaluation (Fig. 3). The C 1 s and N 1 s spectra of $FTCN_{so}$ did not change significantly compared to the original CN and TCN_{iso}, and the assignment of each peak was shown in Fig. 3A and B. All samples showed similar C 1 s and N 1 s spectra, and the assignment of each peak was shown in Fig. 3A and 3B, respectively. In detail, in the C 1 s spectrum, the peaks near binding energies of 287.7 eV, 286.2 eV, and 284.3 eV were assigned to $N - C = N$, $C - O$ and $C - C$ peaks, respectively. Similarly, there were four peaks in the N 1 s spectra of all samples. The peaks near binding energies of 404.2 eV, 401.1 eV, 399.9 eV and 398.3 eV were attributed to π excitation of the heptazine cycles, $N-(C)_3$ and $C - N - H$ peaks, respectively [61]. In addition, the binding energies of C 1 s and N 1 s in $FTCN_{so}$ had some deviations from CN and TCN_{iso}, which might be related to surface modification caused by its special structure [56]. According to the results of S 2p spectrum (Fig. 3E), the peak intensity of the S 2p spectrum in $FTCN_{so}$ was almost the same as the intensity of signal noise, which indicated that the content of S in $FTCN_{so}$ could be ignored. This conclusion was further verified by the strong S 2p peak in the composite material with 5%
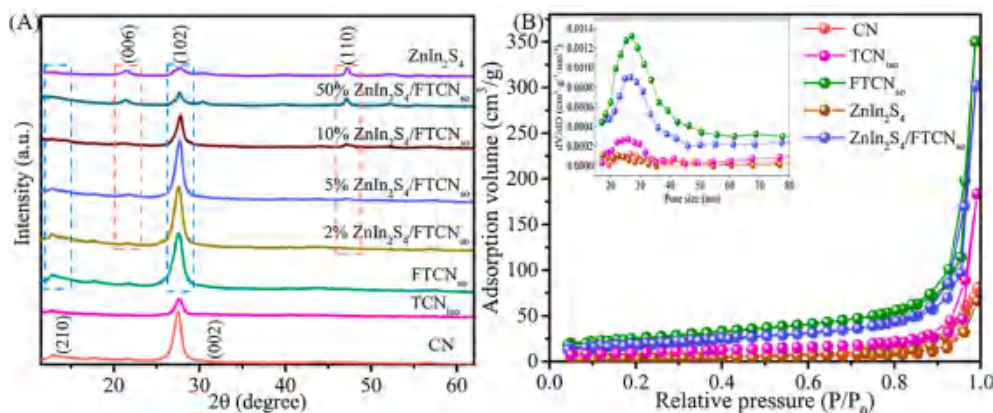

Fig. 2. The XRD patterns of as-prepared samples (A) and the N_2 adsorption and desorption isotherms and pore size distributions of as-prepared samples (B).
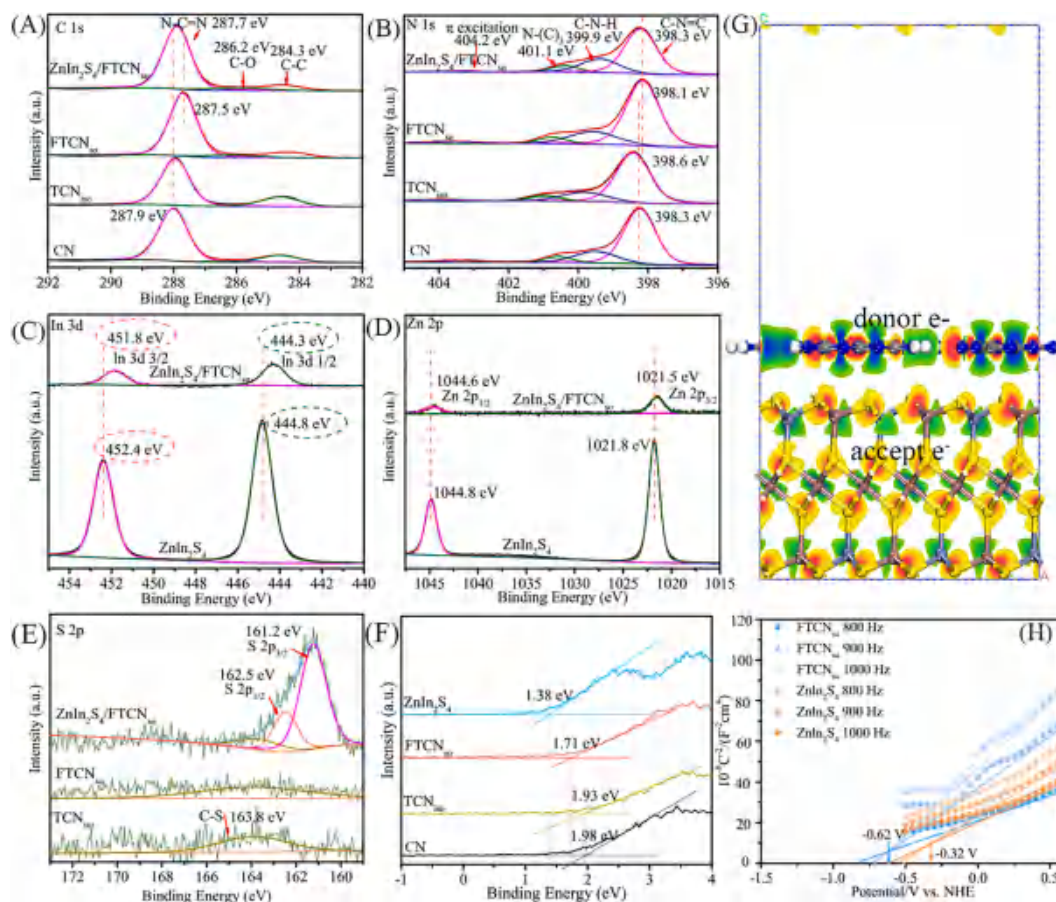
Fig. 3. The XPS spectra of as-prepared samples: C 1 s spectrum (A), N 1 s spectrum (B), ln 3d spectrum (C), Zn 2p spectrum (D), S 2p spectrum (E), and valence band (F). The charge difference density of $ZnIn_2S_4/FTCN_{so}$ (G), and Mott-Schottky plots of $ZnIn_2S_4$ and $FTCN_{so}$ (H).

$ZnIn_2S_4$ content. Therefore, the role of trithiocyanuric acid was to build the skeleton, create pores and defects, rather than introducing S element doping. From another perspective, it could be found that the binding energy of the 1n 3d orbital of the composite material $ZnIn_2S_4/FTCN_{so}$ had moved significantly to the lower field than that of $ZnIn_2S_4$ (Fig. 3A-D), and the similar directional movement occurred on Zn 2p orbital. However, the element binding energy of $FTCN_{so}$ and the $ZnIn_2S_4/FTCN_{so}$ showed the opposite trend. The C 1 s and N 1 s of the $ZnIn_2S_4/FTCN_{so}$ had a small shift to the higher field than that of $FTCN_{so}$. Therefore, the XPS results indicated that there was a strong interaction between $ZnIn_2S_4$ and $FTCN_{so}$ of $ZnIn_2S_4/FTCN_{so}$, which might be due to electron transfer between the two semiconductors [62]. In order to determine the direction of electron transfer, theoretical calculations were used to study the charge differential density of the composite, and the result was shown in Fig. 3G. The electron density of the layer of $FTCN_{so}$ near $ZnIn_2S_4$ decreased, while the electron density of the layer of $ZnIn_2S_4$ near $FTCN_{so}$ increased. In other words, $FTCN_{so}$ acted as an electron donor to transfer electrons to the electron acceptor-$ZnIn_2S_4$. The theoretical calculation results were consistent with the XPS test conclusions. Therefore, $FTCN_{so}$ transferred electrons to $ZnIn_2S_4$ in this system, resulting in a shift in the binding energy of the composite material. Importantly, the strong interface coupling between the two semiconductors could promote the separation and migration of photo-generated carriers, which was beneficial to improve the photocatalytic performance. In addition, in order to better explored the mechanism of electron transfer, the valence bands of several materials were tested through XPS (Fig. 3F). The valence band of the novel $FTCN_{so}$ material moved up significantly compared to CN, which indicated the band gap structure of CN was changed and the photocatalytic performance of the material was affected. The upward shift of the valence band caused the

conduction band to also move upward, which made it easier for substances to produce e^-. The generation of e^- enhanced the conversion of O_2 to O_2^-, and O_2^- as a common active substance will promote the photocatalytic performance of the material, especially for the degradation process where O_2^- was the main active component (Fig. 8B-D). In addition, in order to more accurately explore the photocatalytic mechanism, we also tested the Mott-Schottky curve of $ZnIn_2S_4$ and $FTCN_{so}$ (Fig. 3H). It could be obtained that the flat band potentials of $ZnIn_2S_4$ and $FTCN_{so}$ were −0.62 V and −0.32 V, respectively. For n-type semiconductors, the minimum conduction band (ECBM) was approximately equal to the flat band potential [63].

3.1.2. Optical characteristics and electronic structure analysis

Optical properties are an important factor affecting photocatalytic activity. In this study, UV–vis DRS was used to determine the optical properties of as-prepared samples. As shown in Fig. 4A, all samples exhibited strong absorption of ultraviolet light ($\lambda < 420$ nm), but there was a clear difference to VSL ($\lambda > 420$ nm). The VSL absorption performance of $FTCN_{so}$ was slightly stronger than that of TCN_{iso} and CN, which was attributed to the special structure formed by sufficient self-assembly. In detail, the surface of the $FTCN_{so}$ had a rich void structure, which increased the contact area of visible light, the propagation path strength and the light scattering, resulting in the enhancement of light absorption ability. At the same time, this unique material had a small band gap, which also proved that it had strong visible light absorption [64]. As for $ZnIn_2S_4$, it had strong VSL absorption. Consequently, the heterojunction material had a strong VSL absorption capacity compared to $FTCN_{so}$ due to the existence of $ZnIn_2S_4$. The result was that heterojunction materials easily had strong photo-generated carrier ability under VSL irradiation. Next, the band gap structure of
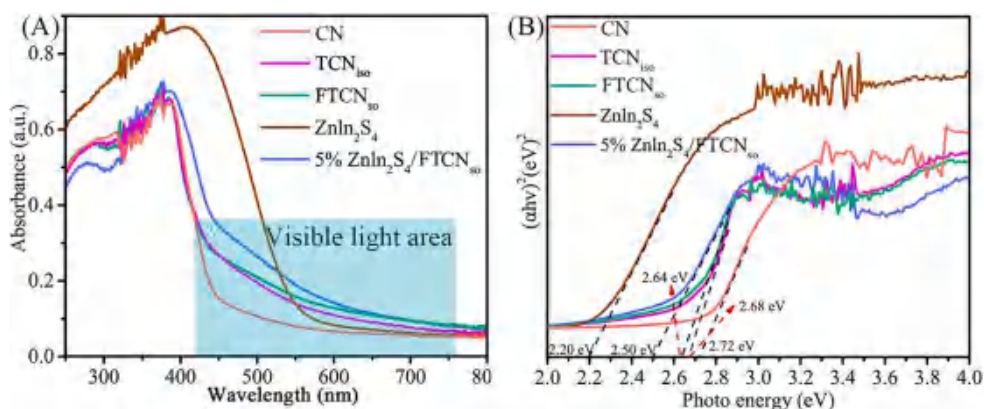
Fig. 4. UV–vis DRS spectrum of as-prepared samples (A); The band gap energies of as-prepared samples calculated by the date of UV–vis DRS spectrum (B).
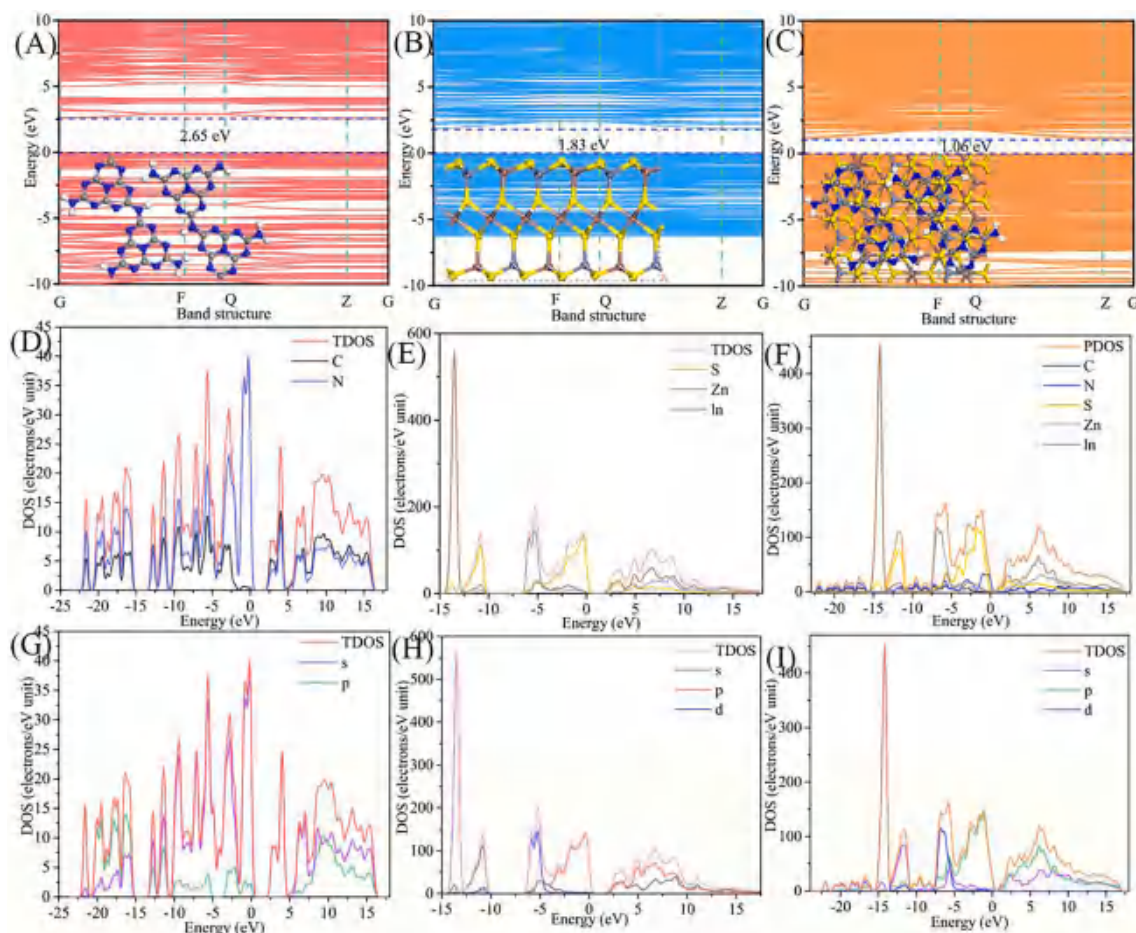

Fig. 5. The band structures and optimal geometric configuration of FTCN$_{so}$, ZnIn$_2$S$_4$ and ZnIn$_2$S$_4$/FTCN$_{so}$ obtained by theoretical calculations (A-C).The TDOS of FTCN$_{so}$ (D, G), ZnIn$_2$S$_4$ (E, H) and ZnIn$_2$S$_4$/FTCN$_{so}$ (F, I) obtained by theoretical calculations.

the material was analyzed. The band gap of FTCN$_{so}$, and ZnIn$_2$S$_4$ were 2.65 eV, and 1.83 eV, calculated by the data of UV–vis DRS (Fig. 4B), respectively, which were consistent with the literature report [36,52,53].

In order to further explore the electronic structure properties of the material, the band gap structure of the material was further analyzed, so the density of states related to it was studied. As for the study of density of states, this article mainly conducted comparative analysis from two aspects, one was the composition of elements, and the other was the type of orbit. As for FTCN$_{so}$ semiconductors (Fig. 5D), valence band top (VBT)

was mainly provided by N atoms, and C atoms occupied most of the conduction band bottom (CBB). Among them, the s orbitals, including C 2 s and N 2 s orbitals, played a major role in the density of states, especially in CBB (Fig. 5G). As for the ZnIn$_2$S$_4$ semiconductor (Fig. 5E), the atoms that make the main contribution to VBT are ln, S, and Zn in order of size, and the ln atom played a leading role with CBB. The ln 3d orbital played the most prominent role, while the p orbital mainly affected CBB (Fig. 5H). Due to the higher orbital energy of ln, the VBT moved upward, which was consistent with the XPS valence band. Similar to ZnIn$_2$S$_4$, for the ZnIn$_2$S$_4$/FTCN$_{so}$ composite material, ln, Zn

and S atoms played a major role. As for VBT, C and N played a relatively weak role (Fig. 5F). The d orbital and p orbital play a decisive role in VBT, and the P orbital also plays a vital role in CBB (Fig. 5I). It was worth noting that the DOS of the $ZnIn_2S_4/FTCN_{so}$ composite material at the Fermi level was significantly higher than that of $ZnIn_2S_4$ and $FTCN_{so}$, which indicated $ZnIn_2S_4/FTCN_{so}$ had a higher carrier mobility than single-component semiconductors [65,66].

3.1.3. Photoelectrochemical performance analysis

In addition to optical properties and band gap structure, photo-electrochemical properties are also an important factor affecting the performance of semiconductor photocatalysts because they reflect the separation and transfer of electrons and holes. The photocurrent was used to evaluate the photoexcited carrier separation of as prepared photocatalysts and photocurrent responses. As shown in Fig. 6A, $ZnIn_2S_4/FTCN_{so}$ exhibited the best photocurrent intensity, indicating that the heterojunction material had the outstanding e^--h^+ separation efficiency and photocurrent responses. This was most likely attributing the presence of structural defects, ordered tubular structure, and wide heterojunction band gap according to the result of photocurrent. Furthermore, the solid steady-state PL spectrum was used to determine the separation efficiency of photogenerated carriers (Fig. 6B). The CN-based photocatalyst had an obvious absorption peak near 465 nm. Meanwhile, the PL spectrum of the modified sample had a certain red shift, which further confirmed that the band gap had changed. The absorption peak position was at 550 nm for $ZnIn_2S_4$. Although the PL spectra of $ZnIn_2S_4$ and $ZnIn_2S_4/FTCN_{so}$ had similar absorption peak intensities, $ZnIn_2S_4/FTCN_{so}$ had a stronger photocurrent response.

For an excellent photocatalyst, it is not only necessary to inhibit the combination of electrons and holes, but also to accelerate the transfer of electrons and holes. The transfer of electrons was measured by electrochemical impedance EIS. As shown in Fig. 6C, the $ZnIn_2S_4/FTCN_{so}$ heterojunction composite had smaller arc than that of other as-prepared samples, indicating that heterojunction composite had the lower carrier

migration resistance and it was beneficial to improve the photocatalytic activity. In short, the heterojunction composite had the highest e^--h^+ separation and transfer efficiency according to the results of photo-electrochemistry, which was conducive to improving the photocatalytic performance [67]. Furthermore, the transient PL was used to observe the electron-hole recombination time intuitively (Fig. 6D). The $ZnIn_2S_4/FTCN_{so}$ composite material had a longer average decay time than a single semiconductor, which indicated that the existence of the heterojunction interface could effectively accelerate the transfer of photo-generated charges and effectively inhibit charge recombination.

3.2. Photocatalytic performance

3.2.1. Photodegradation of TCH

The photocatalytic performance of as-prepared photocatalysts was evaluated by photodegradation of TCH under VSL irradiation, and the result was shown in the Fig. 7A and S2. The adsorption of TCH by $ZnIn_2S_4/FTCN_{so}$ reached equilibrium within 30 min. The adsorption performance of $FTCN_{so}$ was improved compared to the original CN due to the abundant pores. As for the composite heterojunction photo-catalyst, the adsorption performance showed a gradually increasing trend. The maximum adsorption rate of $ZnIn_2S_4$ monomer reached 80% as the content of $ZnIn_2S_4$ increased, which was probably because of the strong metal cation-π interaction between benzene ring in tetracycline and Zn^{2+} in $ZnIn_2S_4$ [40,68]. From the perspective of photocatalytic degradation, the photocatalytic performance of $FTCN_{so}$ was greatly improved compared to TCN_{iso} and CN, which was attributed to its internal ordered structure, abundant structural defects, strong VSL absorption capacity and excellent electrochemical performance according to the results of the above discussions. When only 2% $ZnIn_2S_4$ was compounded, the $ZnIn_2S_4/FTCN_{so}$ heterojunction exhibited a fast degradation rate and high removal rate, which was due to the presence of the heterojunction leading to strong photocatalytic kinetic energy and promoting the separation of e^--h^+. With the gradual increase of $ZnIn_2S_4$
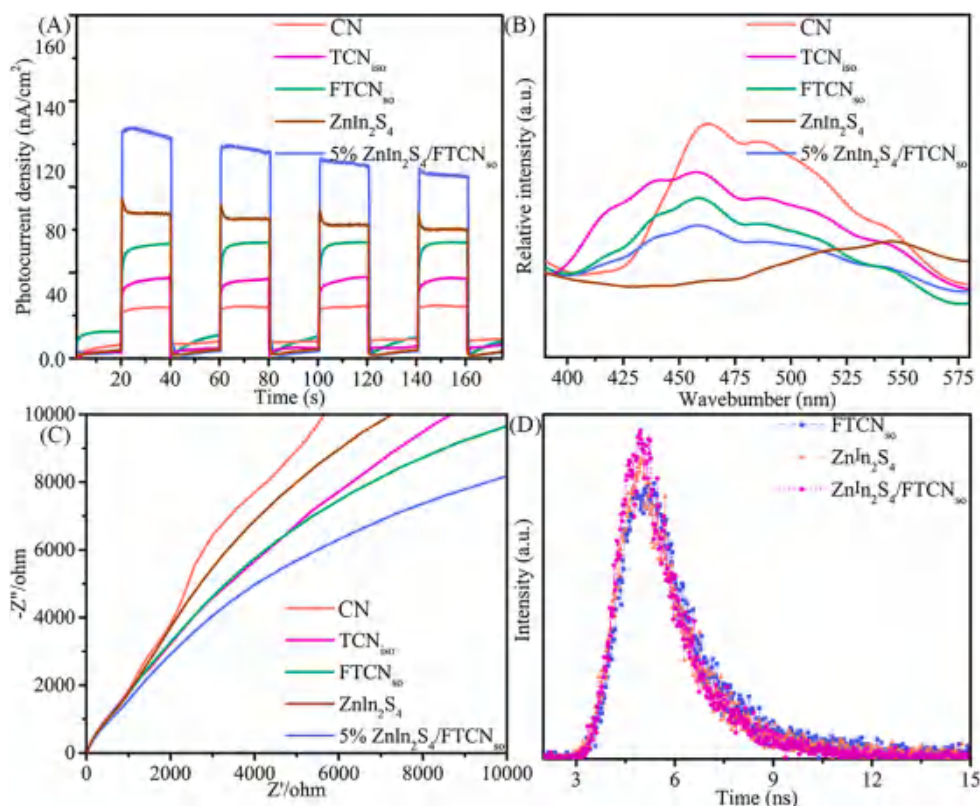

Fig. 6. The photocurrent (A), steady PL (B), EIS (C) of as-prepared samples, and transient PL (D) spectra of the as-prepared samples.
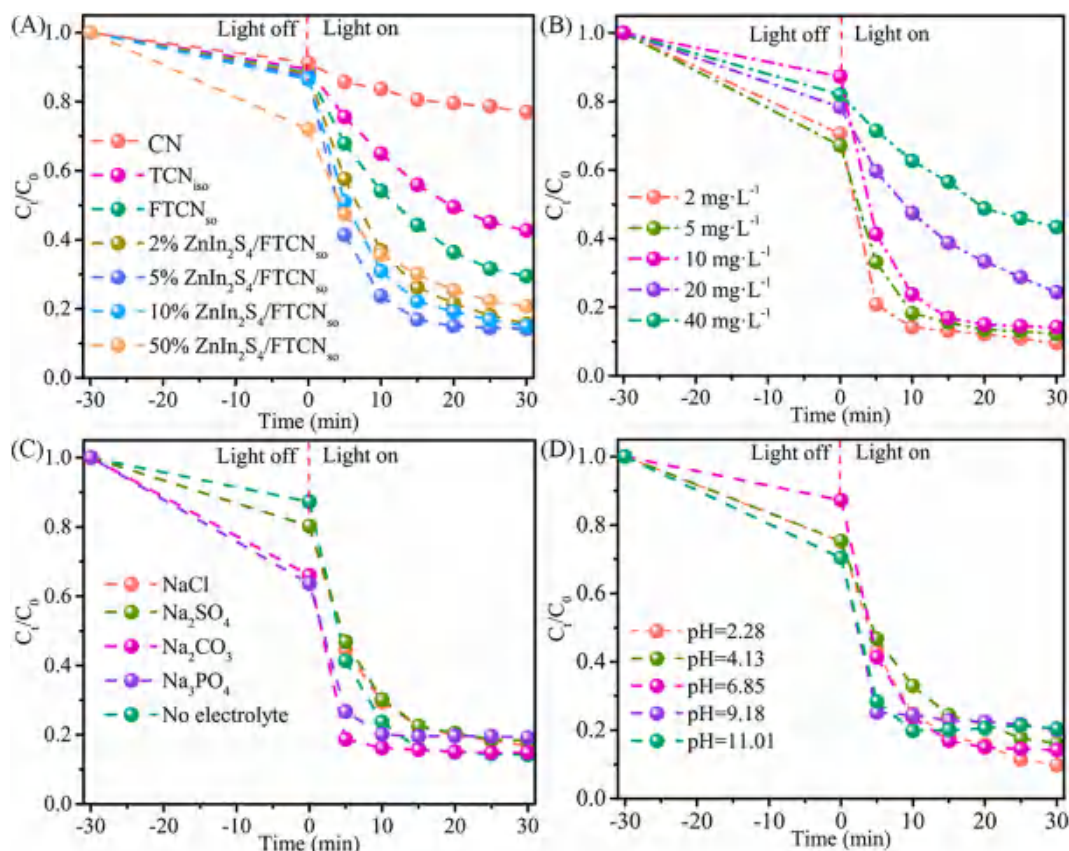
Fig. 7. The photocatalytic activities of as-prepared samples (A); The Effect of initial concentration (B), supporting electrolytes (C), and solution pH (D) for TCH degradation by $ZnIn_2S_4/FTCN_{so}$ under VSL irradiation.
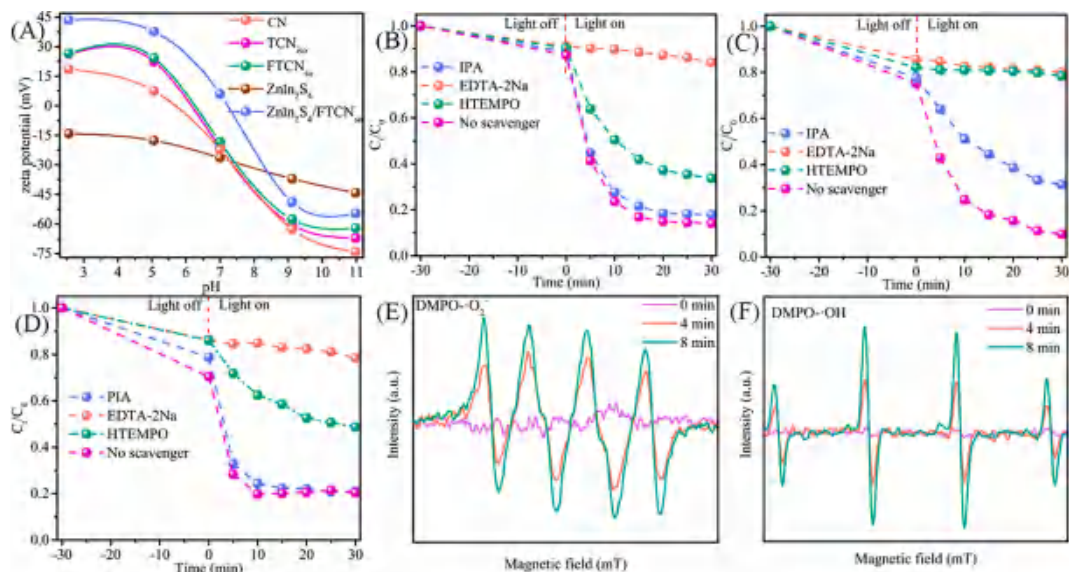

Fig. 8. The Zeta potentials of samples prepared in different pH solution (A). The trapping experiment of radical species during the photocatalytic degradation of TCH by $ZnIn_2S_4/FTCN_{so}$ in acidic solution (pH = 2.58, B), neutral solution (pH = 6.85, C) and alkaline solution (pH = 11.04, D). The ESR spectra of radical adducts trapped by $DMPO·O_2^-$ (E) and $·OH$ (F) in $ZnIn_2S_4/FTCN_{so}$ dispersion.

content to 5%, the overall performance of heterojunction content, thickness, optical and electrochemical properties reached the best according to the results of UV–vis DRS and electrochemistry. As the content of $ZnIn_2S_4$ further increased, excessive deposition on $FTCN_{so}$ might reduce the exposure of active sites and inhibited the generation and transfer of photo-generated charges, reducing the photodegradation

efficiency. Compared with the original CN (14%) and $ZnIn_2S_4$ (17%), the degradation efficiency of 5% $ZnIn_2S_4/FTCN_{so}$ reached 74%. The degradation performance order of all photocatalysts was 5% $ZnIn_2S_4/FTCN_{so}$ (74%) > 10% $ZnIn_2S_4/FTCN_{so}$ (72%) > 2% $ZnIn_2S_4/FTCN_{so}$ (71%) > $FTCN_{so}$ (58%) > 50% $ZnIn_2S_4/FTCN_{so}$ (52%) > 90% $ZnIn_2S_4/FTCN_{so}$ (33%) > TCN_{iso} (31%) > 95% $ZnIn_2S_4/FTCN_{so}$ (21%) > $ZnIn_2S_4$

(17%) > CN (14%). After that, considering the complex environment in actual wastewater, we investigated the effects of antibiotic concentration, electrolyte category and pH type on the degradation of TCH by $ZnIn_2S_4/FTCN_{so}$.

3.2.2. Effects of initial antibiotic concentrations

The degradation performance at different initial concentrations (2–40 mg L^{-1}) was shown in Fig. 7B. With the gradual increase and decrease of the concentration, the degradation rate of 5% $ZnIn_2S_4/FTCN_{so}$ to TCH gradually decreased, which were 91.43%, 87.82%, 85.80%, 75.63%, and 57.65%, respectively. At high pollutant concentrations, the transmission path and light transmittance of photo-generated carriers were reduced, which affected the migration of carriers to the active part of the photocatalyst, reducing its photocatalytic performance [69,70]. Meanwhile, the intermediate product in the process of photocatalytic degradation of TCH compete with TCH molecules for limited photocatalytic active sites, which further led to a decrease in photocatalytic activity [71]. Although high concentration was not conducive to photocatalytic activity, 5% $ZnIn_2S_4/FTCN_{so}$ exhibited excellent photocatalytic performance of TCH removal at low pollutant concentration. Combined with the fact that wastewater often had a low concentration of pollutants, 5% $ZnIn_2S_4/FTCN_{so}$ could be considered as an effective photocatalyst for the degradation of antibiotic TCH.

3.2.3. Effect of supporting electrolytes

Some anions, such as Cl^-, SO_4^{2-}, PO_3^{3-} and CO_3^{2-}, often coexist in the actual water environment. Therefore, by adding NaCl, Na_3PO_3, Na_2SO_4 and Na_2CO_3 (0.05 M), the effect of anions on the photocatalytic removal of TCH by 5% $ZnIn_2S_4/FTCN_{so}$ was studied (Fig. 7C). The addition of Cl^- and SO_4^{2-} had a certain inhibitory effect on the photocatalytic degradation, which might be due to the competitive adsorption between the two anions and TCH [6,72]. However, the addition of CO_3^{2-} and PO_3^{3-} significantly affected the adsorption and photocatalytic degradation efficiency of 5% $ZnIn_2S_4/FTCN_{so}$ on TCH. CO_3^{2-} and PO_3^{3-} are easily hydrolyzed ($CO_3^{2-} + H_2O \rightarrow HCO_3^- + OH^-$, $PO_3^{3-} + H_2O \rightarrow HPO_3^{2-} + OH^-$), and hydrolysis made the solution alkaline. Combined with Fig. 7D and Fig. 8C, 5% $ZnIn_2S_4/FTCN_{so}$ exhibited enhanced adsorption performance for TCH under alkaline conditions. Simultaneously, the main active species were changed under alkaline conditions. All in all, the presence of electrolyte had little effect on the photocatalytic removal of TCH by 5% $ZnIn_2S_4/FTCN_{so}$.

3.2.4. Effects of reaction pH

The reaction pH has always been considered as the main factor affecting the photocatalytic activity. Therefore, the solutions at different pH (2.28, 4.13, 6.85, 9.18, 11.01) were prepared, which were adjusted by NaOH (0.1 M) or HCl (0.1 M). Meanwhile, in order to better analyze the possible mechanism, the Zeta potential of the solution at different pH was measured (Fig. 8A). The results of Zeta potential showed that the negative charges of CN, TCN_{iso}, and $FTCN_{so}$ gradually decrease. This might be due to this special structure. As for $ZnIn_2S_4/FTCN_{so}$, Zeta potential was also increased compared to $FTCN_{so}$ and $ZnIn_2S_4$, which might be related to its obtained under acidic conditions. As shown in Fig. 7D, the photocatalytic degradation performance was little affected and there was no obvious change under acidic conditions. However, it showed a completely different phenomenon in an alkaline environment. The adsorption performance was significantly improved, while the photocatalytic degradation activity was reduced. Combining the photocatalytic Zeta potential and the positively charged characteristics of TCH, we concluded that the electrostatic interaction between the two led to the increase in adsorption performance [73,74].

In order to analyze the effect of pH on the degradation mechanism more clearly, the active ingredients produced in the degradation process of acidic, neutral and alkaline solutions were studied (Fig. 8B-D). Degradation capture experiments at different pH solution showed that pH will affect the role of active species in the degradation process. Common scavengers (1 mmol), 4-hydroxy-TEMPO (HTEMPO, $\cdot O_2^-$ scavenger), isopropanol (IPA, $\cdot OH$ scavenger) and disodium ethyl-enediaminetetraacetic acid (EDTA-2Na, h^+ scavenger) were used [47]. Nevertheless, all experimental results demonstrated that $\cdot O_2^-$ played the most critical component in the degradation process, h^+ was also an exceedingly important role, and $\cdot OH$ had the least impact. Further analysis, the content of $\cdot OH$ increased due to the presence of a large amount of H^+ under acidic conditions. Meanwhile, the presence of OH^- consumed the main active substance h^+ in an alkaline environment, which reduced its impact on photocatalytic degradation performance. In summary, even though the photocatalytic degradation performance under alkaline conditions had decreased, the magnitude of this decrease was very small. Therefore, the photocatalyst had good stability in wastewater with different pH. Meanwhile, the ESR characterization results also confirmed the existence of $\cdot OH$ and $\cdot O_2^-$, and the concentration of active species increased with the increased of VSL irradiation time (Fig. 8E, F).

3.2.5. Mineralization capacity and photostability tests

The photocatalyst can mineralize organic pollution into water, CO_2 and inorganic salts. Therefore, the mineralization ability is an extremely important indicator of the photocatalyst in practical applications. The degree of mineralization of pollutants in different degradation time periods was tested by TOC analyzer. Here, assuming that the TOC in the initial solution of TCH was 100%, the result of the measured TOC was shown in Fig. 9A. The $ZnIn_2S_4/FTCN_{so}$ composite material had good mineralization ability, and the mineralization efficiency of TCH reached 79% under 30 min of VSL irradiation, which had promising application prospects.

An excellent photocatalyst, it needs to have outstanding photocatalytic performance, superior renewable and reusable performance. In order to test the repeated use performance of the photocatalyst, five repeated use experiments were performed on $ZnIn_2S_4/FTCN_{so}$. After each photodegradation cycle, it was filtered, washed with water and ethanol, then dried, and then used in the next cycle experiment. The result of repeated use was shown in Fig. 9B. After 5 times of repeated use, the photodegradation efficiency of $ZnIn_2S_4/FTCN_{so}$ on TCH decreased from 85.8% to 80.3%, which indicated that the catalyst had good repeated use performance. In order to further test the stability of the material, XPS, XRD, SEM and TEM were used to test the photocatalyst after repeated use, and the results were shown in Fig. 10. After enough repeated use, several characterization results were similar to the results before the experiment. The weakening of the intensity and area of XPS and XRD peaks indicated that the content of $ZnIn_2S_4$ in the composite material had a small decrease after repeated use (Fig. 10A-D). Furthermore, the SEM and TEM tests showed that the structure of the material was retained after sufficient use (Fig. 10E-F). Therefore, we could speculate that the loss of part of the heterojunction in some composite materials was an important reason for the reduction of photocatalyst activity. From the analysis of the composition and structure of the composite, the good reusability might be attributed to the $FTCN_{so}$ tubular framework structure and the strong $Zn^{2+}-\pi$ interaction. The above results manifested that the $ZnIn_2S_4/FTCN_{so}$ composite material had excellent mineralized antibiotic TCH ability and reusable performance, and had good application potential in practical applications.

3.2.6. Photocatalytic H_2O_2 production

The photocatalytic production of H_2O_2 was carried out in an aqueous ethanol solution saturated with O_2 (10% vol) under VSL irradiation. The concentration of H_2O_2 over time on different samples was shown in Fig. 11A. The amount of H_2O_2 produced by $ZnIn_2S_4/FTCN_{so}$ was 135.98 $\mu mol\ L^{-1}$, which was significantly higher than that of other photocatalysts. By comparing the H_2O_2 production performance of $FTCN_{so}$ and $ZnIn_2S_4$, it could be inferred that the excellent H_2O_2 production performance of $ZnIn_2S_4/FTCN_{so}$ composites was due to the existence of
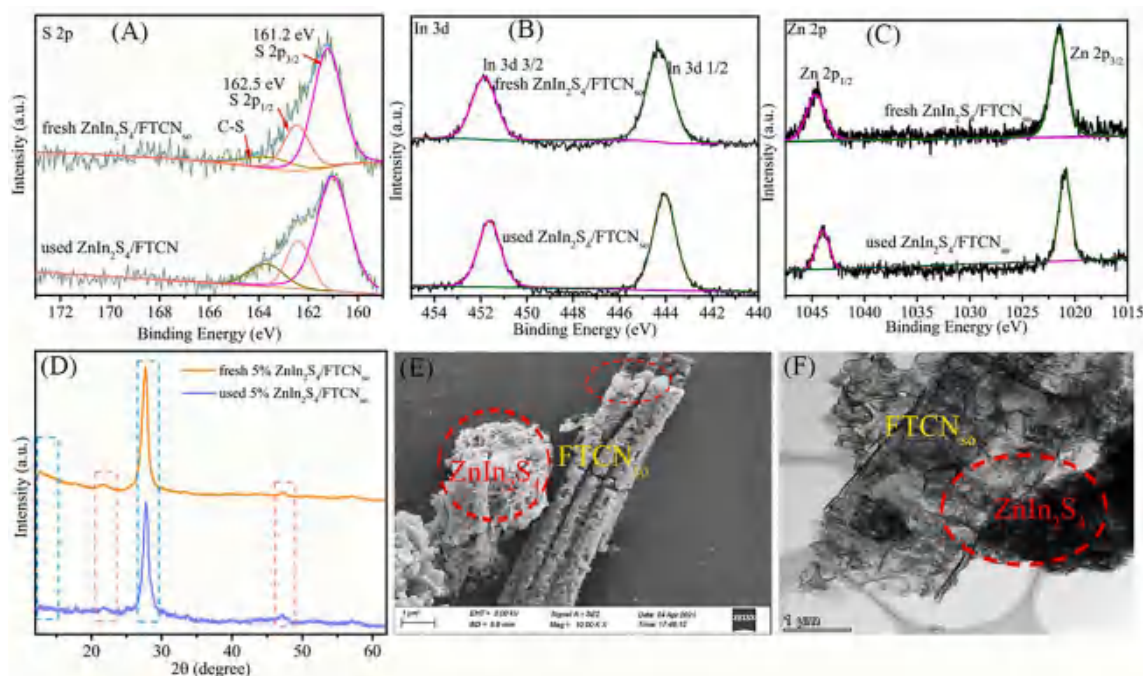
Fig. 9. The XPS spectra of ZnIn$_2$S$_4$/FTCN$_{so}$ before and after used: S 2p spectrum (A), ln 3d spectrum (B) and Zn 2p spectrum (C). The XRD pattern (D), SEM (E) and TEM (F) of ZnIn$_2$S$_4$/FTCN$_{so}$ before and after 5 cycle photocatalytic experiment.
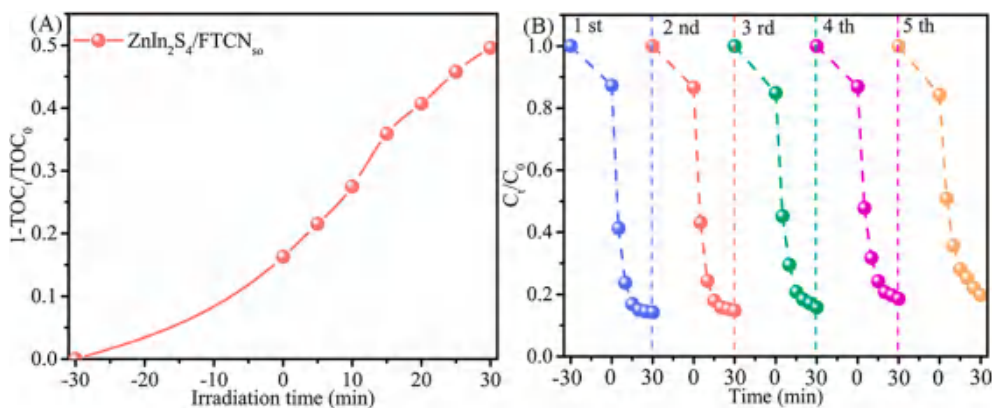

Fig. 10. The TOC removal of TCH by ZnIn$_2$S$_4$/FTCN$_{so}$ composite (A). The cyclic experiments for degrading TCH by ZnIn$_2$S$_4$/FTCN$_{so}$ composite (B).

heterojunction.

H$_2$O$_2$ is often accompanied by decomposition during the production process. In order to clearly analyze the process of ZnIn$_2$S$_4$/FTCN$_{so}$ photocatalytic production of H$_2$O$_2$, the pseudo-first-order kinetic model (Eq. (1)) that could reflect the production rate and decomposition rate was used to fit and analyze the data, and the results were shown in Fig. 11B. The fitted data showed that the K_f of H$_2$O$_2$ produced by FTCN$_{so}$ was significantly lower than that of ZnIn$_2$S$_4$ and ZnIn$_2$S$_4$/FTCN$_{so}$. The introduction of ZnIn$_2$S$_4$ significantly improved the H$_2$O$_2$ production capacity of ZnIn$_2$S$_4$/FTCN$_{so}$. From the analysis of the K_d value, it was known that the K_d of ZnIn$_2$S$_4$/FTCN$_{so}$ was smaller than that of ZnIn$_2$S$_4$ due to the introduction of FTCN$_{so}$ with a small K_d. Therefore, the kinetic results showed that the ZnIn$_2$S$_4$/FTCN$_{so}$ promoted the production of ZnIn$_2$S$_4$ and inhibited its decomposition [10].

$$[H_2O_2] = \frac{K_f}{K_d}(1 - \exp(-K_d t)) \tag{1}$$

In order to further understand the mechanism of photocatalytic H$_2$O$_2$ production, some comparative experiments were carried out on the

H$_2$O$_2$ production (Fig. 11C). The results of the control experiment showed that the H$_2$O$_2$ production was found in the decomposition of water without the addition of sacrificial agent and in the natural state, which indicated that a large amount of H$_2$O$_2$ was also produced in the process of photocatalytic degradation. Moreover, the presence of H$_2$O$_2$ generally helped to improve the performance of photocatalysts in removing pollutants [75]. In the control experiment where nitrogen was introduced into the amine reaction species, part of the H$_2$O$_2$ was still produced under VSL irradiation, which indicated that the production of H$_2$O$_2$ was not only produced by the reduction of O$_2$ by electrons, but also obtained by the oxidation of H$_2$O by photo-generated holes. Based on the above conclusions, the generation of ·OH, e$^-$, h$^+$ could promote the generation of H$_2$O$_2$ and further promote the improvement of photocatalytic degradation performance.

Similarly, repeated use experiments for producing H$_2$O$_2$ were also carried out. The regeneration process of the catalyst was the same as that of the degradation experiment, and 5 repeated use experiments were carried out. As shown in Fig. 11D, after 5 cycles of repeated use, the H$_2$O$_2$ production performance dropped from 135.98 μmol L^{-1} to 104.92
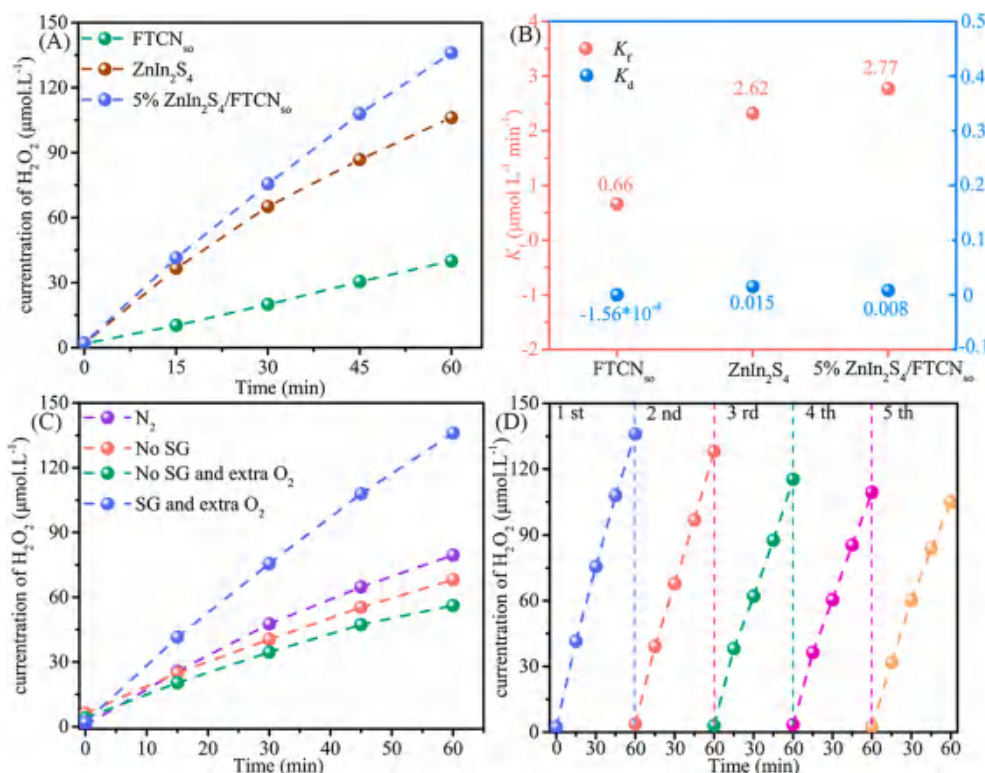
Fig. 11. Photocatalytic H_2O_2 production performance of the prepared material under VSL irradiation (A). The relationship between formation rate constant (K_f) and decomposition rate constant (K_d) for H_2O_2 production (B). The performance of photocatalytic H_2O_2 in complex environments includes the effects of air and sacrificial agents (C). Cycling experiments for the photocatalytic H_2O_2 production by $ZnIn_2S_4/FTCN_{so}$.

μmol L^{-1}, and the high photocatalytic H_2O_2 production performance was still retained. In summary, the $ZnIn_2S_4/FTCN_{so}$ composite heterojunction photocatalyst had excellent photocatalytic performance of H_2O_2 production and degradation of tetracycline, and a large amount of H_2O_2 was generated even in the normal degradation process, which further improved the removal performance of TCH. Therefore, $ZnIn_2S_4/FTCN_{so}$ was a promising photocatalyst for degrading pollutants and producing H_2O_2.

3.3. Photocatalytic mechanism

In the previous part, we explored the active species of $\cdot O_2^-$, $\cdot OH$ and

h^+ in the photocatalytic degradation of TCH by $ZnIn_2S_4/FTCN_{so}$ by studying active species capture experiments at different pH solution. In order to further analyze the mechanism of photocatalysis, it is necessary to analyze the transfer mechanism of electrons and holes. To study the relationship between the semiconductor valence band, conduction band and band gap requires a combination of various technologies.

The band gaps of $ZnIn_2S_4$ and $FTCN_{so}$ were obtained according to UV–vis, which were 2.20 eV and 2.64 eV. According to the Mott-Schottky curves, the E_{CBM} of $ZnIn_2S_4$ and $FTCN_{so}$ could be calculated to be -0.32 eV and -0.62 eV, respectively. The maximum valence band (E_{VBM}) of $ZnIn_2S_4$ and $FTCN_{so}$ calculated by Eq. (2) is -1.88 V and -2.02 V, respectively. Meanwhile, the valence bands of $ZnIn_2S_4$ and
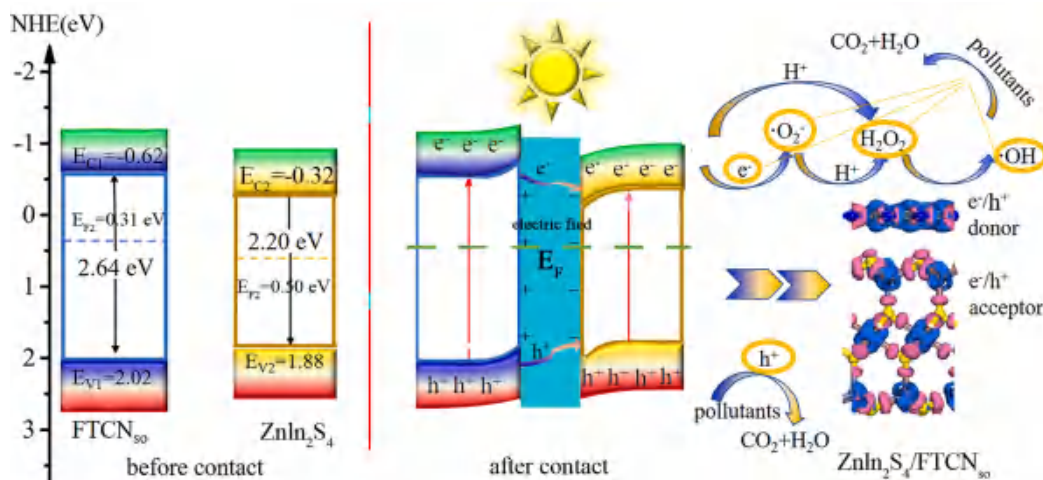

Fig. 12. The proposed mechanism of band structure and charge separation at the interface in the $ZnIn_2S_4/FTCN_{so}$ isotype heterojunction structure under VSL illumination.
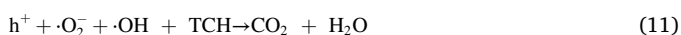
FTCN$_{so}$ were obtained by XPS, which are 1.38 eV and 1.71 eV, respectively. Because the energy difference between the VB through the XPS test and E$_{VBM}$ obtained was equal to the Fermi level [63]. Therefore, the Fermi levels of ZnIn$_2$S$_4$ and FTCNso were 0.50 V (vs NHE) and 0.31 V (vs NHE), respectively. When semiconductors with different Fermi energy levels are in contact, the Fermi energy levels will tend to be the same, which causes the CB and the VB to be distorted [63,76], and the band gap structure of the two semiconductors was shown in Fig. 12.

The conduction band of FTCN$_{so}$ was higher than that of ZnIn$_2$S$_4$, resulting in the migration of photogenerated electrons from ZnIn$_2$S$_4$ to the valence band of ZnIn$_2$S$_4$, which was consistent with the conclusions of XPS and charge differential density. Similarly, the valence band of FTCN$_{so}$ was more positive than that of ZnIn$_2$S$_4$, resulting in the transfer of holes from the valence band of FTCN$_{so}$ to the valence band of ZnIn$_2$S$_4$. The electron-hole transport contributed to the formation of the type-I binary heterojunction in this way, which provided a fast electron-hole transport channel. Both semiconductors could generate electrons and holes when excited under VSL irradiation.

$$E_{VBM} = E_{CBM} + E_g \qquad (2)$$

After analyzing the band gap structure information of the two semiconductors, it was combined with the potential of active oxygen ($\cdot O_2^-$, $\cdot OH$) to further analyze the material's ability to produce active oxygen. According to the position information of the valence band and conduction band, the ability of ZnIn$_2$S$_4$/FTCN$_{so}$ to generate capture components was deduced. The edge potential of the conduction band of ZnIn$_2$S$_4$ and FTCN$_{so}$ was greater than the potential of O$_2$/$\cdot O_2^-$ (-0.33 eV), which led to the electrons on CB of FTCN$_{so}$ participate in the process of O$_2$ reduction to $\cdot O_2^-$. Due to the fact that both semiconductor materials could produce $\cdot O_2^-$, and $\cdot O_2^-$ was an important way for H$_2$O$_2$ production, which led to the ZnIn$_2$S$_4$/FTCN$_{so}$ heterojunction composite material with excellent H$_2$O$_2$ generation properties. However, the valence edge potential of ZnIn$_2$S$_4$ and FTCN$_{so}$ was more negative than that of OH$^-$/ $\cdot OH$ (2.40 eV) and H$_2$O/$\cdot OH$ (2.72 eV), resulting in that it did not have the ability to directly produce $\cdot OH$. Based on the fact that $\cdot OH$ could not be directly produced, $\cdot OH$ had a weak effect in the degradation process, which was consistent with the conclusion of the active species capture experiment.

In short, due to the synergy between the strong VSL absorption performance of ZnIn$_2$S$_4$ and the rich in structural defects of FTCN$_{so}$, ZnIn$_2$S$_4$/FTCN$_{so}$ had high photocatalytic performance and could effectively photocatalytically degrade TCH and produce H$_2$O$_2$. The main possible reactions of the ZnIn$_2$S$_4$/FTCN$_{so}$ photocatalytic system to the photocatalytic degradation of TCH and the production of H$_2$O$_2$ were as follows:

$$ZnIn_2S_4/FTCN_{so} + VSL \rightarrow ZnIn_2S_4/FTCN_{so}\ (e^-/h^+) \qquad (3)$$

$$h^+ + OH^- \rightarrow \cdot OH \qquad (4)$$

$$e^- + O_2 \rightarrow \cdot O_2^- \qquad (5)$$

$$\cdot O_2^- + H^+ \rightarrow \cdot OOH \qquad (6)$$

$$\cdot OOH + H^+ + e^- \rightarrow H_2O_2 \qquad (7)$$

$$H_2O + h^+ \rightarrow \cdot OH \qquad (8)$$

$$2 \cdot OH \rightarrow H_2O_2 \qquad (9)$$

$$H_2O_2 + e^- \rightarrow \cdot OH + OH^- \qquad (10)$$

$$h^+ + \cdot O_2^- + \cdot OH + TCH \rightarrow CO_2 + H_2O \qquad (11)$$

4. Conclusions

In this article, we succeeded in a novel fish-scale tubular carbon nitride FTCN$_{so}$ with abundant structural defects, and synthesized the ZnIn$_2$S$_4$/FTCN$_{so}$ heterojunction complex on this basis. The novel FTCN$_{so}$ photocatalyst prepared under the dissolution conditions has a significant improvement, which is mainly attributed to the regular structure and abundant structural defects. The further constructed ZnIn$_2$S$_4$/ FTCN$_{so}$ heterojunction has better performance in photocatalytic degradation of TCH (84.3%, 30 min) and H$_2$O$_2$ production (135.98 μmol L^{-1}, 60 min) than that of ZnIn$_2$S$_4$ and FTCN$_{so}$, which is mainly due to the formation of the heterojunction and the synergy between the two semiconductors, resulting in enhanced VSL absorption and electron-hole separation efficiency. In addition, in order to have a deeper understanding of the nature and mechanism of the photocatalysts, the electronic structure properties and charge differential density of the material were further analyzed and explored through theoretical calculations. Furthermore, the mechanism of action of active species (h$^+$, $\cdot O_2^-$ and $\cdot H$) in different pH solutions was explored. Meanwhile, Experiments in complex environments and repeated use showed that the material had good stability. This research can provide new insights for the construction of novel and efficient CN-based photocatalysts under VSL, and promote its practical application in environmental restoration and clean energy.

Declaration of Competing Interest

The authors declare that they have no known competing financial interests or personal relationships that could have appeared to influence the work reported in this paper.

Appendix A. Supplementary data

Supplementary data to this article can be found online at https://doi. org/10.1016/j.cej.2021.130831.

References

[1] Q. He, P. Xu, C. Zhang, G. Zeng, Z. Liu, D. Wang, W. Tang, H. Dong, X. Tan, A. Duan, Influence of surfactants on anaerobic digestion of waste activated sludge: acid and methane production and pollution removal, Crit. Rev. Biotechnol. 39 (2019) 746–757.

[2] S. Xiao, M. Cheng, H. Zhong, Z. Liu, Y. Liu, X. Yang, Q. Liang, Iron-mediated activation of persulfate and peroxymonosulfate in both homogeneous and heterogeneous ways: a review, Chem. Eng. J. 384 (2020), 123265.

[3] J. Huang, X. Liu, W. Zhang, Z. Liu, H. Zhong, B. Shao, Q. Liang, Y. Liu, W. Zhang, Q. He, Functionalization of covalent organic frameworks by metal modification: construction, properties and applications, Chem. Eng. J. 404 (2021), 127136.

[4] W. Zhang, Z. Zeng, Z. Liu, J. Huang, R. Xiao, B. Shao, Y. Liu, Y. Liu, W. Tang, G. Zeng, J. Gong, Q. He, Effects of carbon nanotubes on biodegradation of pollutants: positive or negative? Ecotoxicol. Environ. Saf. 189 (2020) 109914, https://doi.org/10.1016/j.ecoenv.2019.109914.

[5] B. Shao, Z. Liu, G. Zeng, Y. Liu, X. Yang, C. Zhou, M. Chen, Y. Liu, Y. Jiang, M. Yan, Immobilization of laccase on hollow mesoporous carbon nanospheres: noteworthy immobilization, excellent stability and efficacious for antibiotic contaminants removal, J. Hazard. Mater. 362 (2019) 318–326.

[6] B. Shao, X. Liu, Z. Liu, G. Zeng, W. Zhang, Q. Liang, Y. Liu, Q. He, X. Yuan, D. Wang, S. Luo, S. Gong, Synthesis and characterization of 2D/0D g-C$_3$N$_4$/CdS-nitrogen doped hollow carbon spheres (NHCs) composites with enhanced visible light photodegradation activity for antibiotic, Chem. Eng. J. 374 (2019) 479–493.

[7] Z. Peng, X. Liu, W. Zhang, Z. Zeng, Z. Liu, C. Zhang, Y. Liu, B. Shao, Q. Liang, W. Tang, X. Yuan, Advances in the application, toxicity and degradation of carbon nanomaterials in environment: a review, Environ Int 134 (2020) 105298, https://doi.org/10.1016/j.envint.2019.105298.

[8] Y. Liu, H. Cheng, M. Cheng, Z. Liu, D. Huang, G. Zhang, B. Shao, Q. Liang, S. Luo, T. Wu, S.a. Xiao, The application of Zeolitic imidazolate frameworks (ZIFs) and their derivatives based materials for photocatalytic hydrogen evolution and pollutants treatment, Chem. Eng. J. 417 (2021) 127914, https://doi.org/10.1016/j.cej.2020.127914.

[9] M. Zhang, L. He, T. Shi, R. Zha, Neat 3D C3N4 monolithic aerogels embedded with carbon aerogels via ring-opening polymerization with high photoreactivity, Appl. Catal. B, Environ., 266, 2020, 118652.

[10] Y. Yang, Z. Zeng, G. Zeng, D. Huang, R. Xiao, C. Zhang, C. Zhou, W. Xiong, W. Wang, M. Cheng, W. Xue, H. Guo, X. Tang, D. He, Ti3C2 Mxene/porous g-C3N4 interfacial Schottky junction for boosting spatial charge separation in photocatalytic H2O2 production, Appl. Catal. B, Environ. 258 (2019) 117956, https://doi.org/10.1016/j.apcatb.2019.117956.

[11] Z. Jiang, L. Wang, J. Lei, Y. Liu, J. Zhang, Photo-Fenton degradation of phenol by CdS/rGO/Fe^{2+} at natural pH with in situ-generated H2O2, Appl. Catal. B, Environ. 241 (2019) 367–374.

[12] T. Wu, X. Liu, Y. Liu, M. Cheng, Z. Liu, G. Zeng, B. Shao, Q. Liang, W. Zhang, Q. He, W. Zhang, Application of QD-MOF composites for photocatalysis: energy production and environmental remediation, Coord. Chem. Rev. 403 (2020) 213097, https://doi.org/10.1016/j.ccr.2019.213097.

[13] B. Shao, J. Wang, Z. Liu, G. Zeng, L. Tang, Q. Liang, Q. He, T. Wu, Y. Liu, X. Yuan, Ti3C2Tx MXene decorated black phosphorus nanosheets with improved visible-light photocatalytic activity: experimental and theoretical studies, J. Mater. Chem. A 8 (10) (2020) 5171–5185.

[14] Y. Pan, X. Liu, W. Zhang, Z. Liu, G. Zeng, B. Shao, Q. Liang, Q. He, X. Yuan, D. Huang, M. Chen, Advances in photocatalysis based on fullerene C60 and its derivatives: properties, mechanism, synthesis, and applications, Appl. Catal. B, Environ. 265 (2020) 118579, https://doi.org/10.1016/j.apcatb.2019.118579.

[15] Y. Liu, D. Huang, M. Cheng, Z. Liu, C. Lai, C. Zhang, C. Zhou, W. Xiong, L. Qin, B. Shao, Q. Liang, Metal sulfide/MOF-based composites as visible-light-driven photocatalysts for enhanced hydrogen production from water splitting, Coord. Chem. Rev. 409 (2020), 213220.

[16] L. Sun, L. Xiang, X. Zhao, C.-J. Jia, J. Yang, Z. Jin, X. Cheng, W. Fan, Enhanced visible-light photocatalytic activity of bioi/biocl heterojunctions: key role of crystal facet combination, ACS Catal. 5 (2015) 3540–3551.

[17] Y. Fang, Y. Xu, X. Li, Y. Ma, X. Wang, Coating polymeric carbon nitride photoanodes on conductive Y:ZnO nanorod arrays for overall water splitting, Angew. Chem. Int. Ed. 57 (31) (2018) 9749–9753.

[18] T. Wu, P. Niu, Y. Yang, L.-C. Yin, J. Tan, H. Zhu, J.T.S. Irvine, L. Wang, G. Liu, H.-M. Cheng, Homogeneous Doping of substitutional nitrogen/carbon in TiO2 plates for visible light photocatalytic water oxidation, Adv. Funct. Mater. 29 (25) (2019) 1901943, https://doi.org/10.1002/adfm.v29.2510.1002/adfm.201901943.

[19] S. Guo, Z. Deng, M. Li, B. Jiang, C. Tian, Q. Pan, H. Fu, Phosphorus-doped carbon nitride tubes with a layered micro-nanostructure for enhanced visible-light photocatalytic hydrogen evolution, Angew. Chem. Int. Ed. 55 (2016) 1830–1834.

[20] B. Shao, Z. Liu, G. Zeng, Y. Liu, Q. Liang, Q. He, T. Wu, Y. Pan, J. Huang, Z. Peng, S. Luo, C. Liang, X. Liu, S. Tong, J. Liang, Synthesis of 2D/2D CoAl-LDHs/Ti3C2Tx Schottky-junction with enhanced interfacial charge transfer and visible-light photocatalytic performance, Appl. Catal. B, Environ. 286 (2021) 119867, https://doi.org/10.1016/j.apcatb.2020.119867.

[21] B. Shao, X. Liu, Z. Liu, G. Zeng, Q. Liang, C. Liang, Y. Cheng, W. Zhang, Y. Liu, S. Gong, A novel double Z-scheme photocatalyst Ag3PO4/Bi2S3/Bi2O3 with enhanced visible-light photocatalytic performance for antibiotic degradation, Chem. Eng. J. 368 (2019) 730–745.

[22] N. Tian, Y. Zhang, X. Li, K. Xiao, X. Du, F. Dong, G.I.N. Waterhouse, T. Zhang, H. Huang, Precursor-reforming protocol to 3D mesoporous g-C3N4 established by ultrathin self-doped nanosheets for superior hydrogen evolution, Nano Energy 38 (2017) 72–81.

[23] X. Ding, Y. Li, J. Zhao, Y. Zhu, Y. Li, W. Deng, C. Wang, Enhanced photocatalytic H-2 evolution over CdS/Au/g-C3N4 composite photocatalyst under visible-light irradiation, Apl. Materials 3 (2015), 104410.

[24] Y. Luo, B. Deng, Y. Pu, A. Liu, J. Wang, K. Ma, F. Gao, B. Gao, W. Zou, L. Dong, Interfacial coupling effects in g-C3N4/SrTiO3 nanocomposites with enhanced H2 evolution under visible light irradiation, Appl. Catal. B, Environ. 247 (2019) 1–9.

[25] J. Di, J. Xia, X. Li, M. Ji, H. Xu, Z. Chen, H. Li, Constructing confined surface carbon defects in ultrathin graphitic carbon nitride for photocatalytic free radical manipulation, Carbon 107 (2016) 1–10.

[26] P.o. Wu, J. Wang, J. Zhao, L. Guo, F.E. Osterloh, Structure defects in g-C3N4 limit visible light driven hydrogen evolution and photovoltage, J. Mater. Chem. A 2 (47) (2014) 20338–20344.

[27] Z. Zhu, X.u. Tang, T. Wang, W. Fan, Z. Liu, C. Li, P. Huo, Y. Yan, Insight into the effect of co-doped to the photocatalytic performance and electronic structure of g-C3N4 by first principle, Appl. Catal. B, Environ. 241 (2019) 319–328.

[28] Q. Liang, B. Shao, S. Tong, Z. Liu, L. Tang, Y. Liu, M. Cheng, Q. He, T. Wu, Y. Pan, J. Huang, Z. Peng, Recent advances of melamine self-assembled graphitic carbon nitride-based materials: design, synthesis and application in energy and environment, Chem. Eng. J. 405 (2021) 126951, https://doi.org/10.1016/j.cej.2020.126951.

[29] W. Wang, Q. Niu, G. Zeng, C. Zhang, D. Huang, B. Shao, C. Zhou, Y. Yang, Y. Liu, H. Guo, W. Xiong, L. Lei, S. Liu, H. Yi, S. Chen, X. Tang, 1D porous tubular g-C3N4 capture black phosphorus quantum dots as 1D/0D metal-free photocatalysts for oxytetracycline hydrochloride degradation and hexavalent chromium reduction,

[30] M. Tahir, C. Cao, F.K. Butt, F. Idrees, N. Mahmood, Z. Ali, I. Aslam, M. Tanveer, M. Rizwan, T. Mahmood, Tubular graphitic-C3N4: a prospective material for energy storage and green photocatalysis, J. Mater. Chem. A 1 (44) (2013) 13949, https://doi.org/10.1039/c3ta13291a.

[31] Y.-S. Jun, E.Z. Lee, X. Wang, W.H. Hong, G.D. Stucky, A. Thomas, From melamine-cyanuric acid supramolecular aggregates to carbon nitride hollow spheres, Adv. Funct. Mater. 23 (2013) 3661–3667.

[32] C. Zhao, Z. Liao, W. Liu, F. Liu, J. Ye, J. Liang, Y. Li, Carbon quantum dots modified tubular g-C3N4 with enhanced photocatalytic activity for carbamazepine elimination: mechanisms, degradation pathway and DFT calculation, J. Hazard. Mater. 381 (2020).

[33] C. Zhang, Y. Zhou, W. Wang, Y. Yang, C. Zhou, L. Wang, L. Lei, D. He, H. Luo, D. Huang, Formation of Mo2C/hollow tubular g-C3N4 hybrids with favorable charge transfer channels for excellent visible-light-photocatalytic performance, Appl. Surf. Sci. 527 (2020) 146757, https://doi.org/10.1016/j.apsusc.2020.146757.

[34] Z. Tong, D. Yang, Y. Sun, Y. Nan, Z. Jiang, Tubular g-C3N4 Isotype heterojunction: enhanced visible-light photocatalytic activity through cooperative manipulation of oriented electron and hole transfer, Small 12 (2016) 4093–4101.

[35] Z. Gao, K. Chen, L. Wang, B. Bai, H. Liu, Q. Wang, Aminated flower-like ZnIn2S4 coupled with benzoic acid modified g-C3N4 nanosheets via covalent bonds for ameliorated photocatalytic hydrogen generation, Appl. Catal. B, Environ., 268, 2020, 118462.

[36] Y. Qin, H. Li, J. Lu, Y. Feng, F. Meng, C. Ma, Y. Yan, M. Meng, Synergy between van der waals heterojunction and vacancy in ZnIn2S4/g-C3N4 2D/2D photocatalysts for enhanced photocatalytic hydrogen evolution, Appl. Catal. B, Environ. 277 (2020) 119254, https://doi.org/10.1016/j.apcatb.2020.119254.

[37] P. Qiu, J. Yao, H. Chen, F. Jiang, X. Xie, Enhanced visible-light photocatalytic decomposition of 2,4-dichlorophenoxyacetic acid over ZnIn2S4/g-C3N4 photocatalyst, J. Hazard. Mater. 317 (2016) 158–168.

[38] Y. Chen, G. Tian, Z. Ren, K. Pan, Y. Shi, J. Wang, H. Fu, Hierarchical core-shell carbon nanofiber@ZnIn2S4 composites for enhanced hydrogen evolution performance, ACS Appl. Mater. Interfaces. 6 (16) (2014) 13841–13849.

[39] S. Peng, P. Zhu, S.G. Mhaisalkar, S. Ramakrishna, Self-supporting three-dimensional ZnIn2S4/PVDF–Poly(MMA-co-MAA) composite mats with hierarchical nanostructures for high photocatalytic activity, J. Mater. Chem. C 116 (26) (2012) 13849–13857.

[40] X. Xiao, H. Chen, X. Dong, D. Ren, Q. Deng, D. Wang, W. Tian, A double cation-pi-driven strategy enabling two-dimensional supramolecular polymers as efficient catalyst carriers, Angew. Chem. Int. Ed. Engl. 9534–9541 (2020).

[41] S. Yamada, Cation−π interactions in organic synthesis, Chem. Rev. 118 (2018) 11353–11432.

[42] H. Yang, R. Cao, P. Sun, J. Yin, S. Zhang, X. Xu, Constructing electrostatic self-assembled 2D/2D ultra-thin ZnIn2S4/protonated g-C3N4 heterojunctions for excellent photocatalytic performance under visible light, Appl. Catal. B, Environ., 256, 2019, 117862.

[43] B. Lin, H. Li, H. An, W. Hao, J. Wei, Y. Dai, C. Ma, G. Yang, Preparation of 2D/2D g-C3N4 nanosheet@ZnIn2S4 nanoleaf heterojunctions with well -designed high-speed charge transfer nanochannels towards high efficiency photocatalytic hydrogen evolution, Appl. Catal. B, Environ. 220 (2018) 542–552.

[44] F. Guo, Y. Cai, W. Guan, H. Huang, Y. Liu, Graphite carbon nitride/ZnIn2S4 heterojunction photocatalyst with enhanced photocatalytic performance for degradation of tetracycline under visible light irradiation, J. Phys. Chem. Solids 110 (2017) 370–378.

[45] G.P. Zhang, D.Y. Chen, N.J. Li, Q.F. Xu, H. Li, J.H. He, J.M. Lu, Construction of hierarchical hollow Co9S8/ZnIn2S4 tubular heterostructures for highly efficient solar energy conversion and environmental remediation, Angew. Chem. Int. Ed. 59 (2020) 8255–8261.

[46] Z. Tong, D. Yang, Z. Li, Y. Nan, F. Ding, Y. Shen, Z. Jiang, Thylakoid-inspired multishell g-C3N4 nanocapsules with enhanced visible-light harvesting and electron transfer properties for high-efficiency photocatalysis, ACS Nano 11 (1) (2017) 1103–1112.

[47] Q. Liang, X. Liu, J. Wang, Y. Liu, Z. Liu, L. Tang, B. Shao, W. Zhang, S. Gong, M. Cheng, Q. He, C. Feng, In-situ self-assembly construction of hollow tubular g-C3N4 isotype heterojunction for enhanced visible-light photocatalysis: experiments and theories, J. Hazard. Mater. 401 (2021) 123355, https://doi.org/10.1016/j.jhazmat.2020.123355.

[48] G. Zhang, X. Zhu, D. Chen, N. Li, Q. Xu, H. Li, J. He, H. Xu, J. Lu, Hierarchical Z-scheme g-C3N4/Au/ZnIn2S4 photocatalyst for highly enhanced visible-light photocatalytic nitric oxide removal and carbon dioxide conversion, Environ.-Sci Nano 7 (2) (2020) 676–687.

[49] C. Feng, L. Tang, Y. Deng, J. Wang, J. Luo, Y. Liu, X. Ouyang, H. Yang, J. Yu, J. Wang, Synthesis of leaf-vein-like g-C3N4 with tunable band structures and charge transfer properties for selective photocatalytic H2O2 evolution, Adv. Funct. Mater. (2020).

[50] M.P. Zhuo, J.J. Wu, X.D. Wang, Y.C. Tao, Y. Yuan, L.S. Liao, Hierarchical self-assembly of organic heterostructure nanowires, Nat. Commun 10 (2019) 3839.

[51] F.K. Kessler, Y. Zheng, D. Schwarz, C. Merschjann, W. Schnick, X.C. Wang, M. J. Bojdys, Functional carbon nitride materials design strategies for electrochemical devices, Nat. Rev. Mater. 2 (2017) 17030.

[52] Y. Tong, C. Wei, Y. Li, Y. Zhang, W. Lin, Unraveling the mechanisms of S-doped carbon nitride for photocatalytic oxygen reduction to H2O2, PCCP 22 (2020) 21099–21107.

[53] H. Wang, Y. Bian, J. Hu, L. Dai, Highly crystalline sulfur-doped carbon nitride as photocatalyst for efficient visible-light hydrogen generation, Appl. Catal. B, Environ. 238 (2018) 592–598.

[54] S. Wang, F. Zhang, J.B. Fan, Interfacial polymerization: from chemistry to functional materials, Angew. Chem. Int. Ed. Engl. 21840–21856 (2020).

[55] B. Lin, H. An, X. Yan, T. Zhang, J. Wei, G. Yang, Fish-scale structured g-C3N4 nanosheet with unusual spatial electron transfer property for high-efficiency photocatalytic hydrogen evolution, Appl. Catal. B, Environ. 210 (2017) 173–183.

[56] X. Yang, L. Tian, X. Zhao, H. Tang, Q. Liu, G. Li, Interfacial optimization of g-C3N4-based Z-scheme heterojunction toward synergistic enhancement of solar-driven photocatalytic oxygen evolution, Appl. Catal. B, Environ. 244 (2019) 240–249.

[57] S. Babar, N. Gayade, H. Shinde, P. Mahajan, K.H. Lee, N. Mane, A. Deshmukh, K. Garadkar, V. Bhuse, Evolution of waste iron rust into magnetically separable g-C3N4-Fe2O3 photocatalyst: an efficient and economical waste management approach, ACS Appl. Nano Mater. 1 (2018) 4682–4694.

[58] W. Gao, L. Wang, C. Gao, J.Q. Liu, Y. Yang, L.Q. Yang, Q. Shen, C.P. Wu, Y. Zhou, Z.G. Zou, Exquisite design of porous carbon microtubule-scaffolding hierarchical In2O3-ZnIn2S4 heterostructures toward efficient photocatalytic conversion of CO(2) into CO, Nanoscale 12 (2020) 14676–14681.

[59] H.H. Ou, P.J. Yang, L.H. Lin, M. Anpo, X.C. Wang, Carbon nitride aerogels for the photoredox conversion of water, Angew. Chem. Int. Ed. 56 (2017) 10905–10910.

[60] F. Fina, S.K. Callear, G.M. Carins, J.T.S. Irvine, Structural investigation of graphitic carbon nitride via XRD and neutron diffraction, Chem. Mater. 27 (2015) 2612–2618.

[61] Q. Deng, G. Ba, T. Huo, H. Li, W. Hou, Atomic carbon chain-linked polymeric carbon nitride: roles of the carbon chain in enhancing the photocatalytic hydrogen evolution performance, Applied Catalysis A: General 606 (2020), 117833.

[62] D. Zeng, L. Xiao, W.-J. Ong, P. Wu, H. Zheng, Y. Chen, D.-L. Peng, Hierarchical ZnIn2S4/MoSe2 nanoarchitectures for efficient noble-metal-free photocatalytic hydrogen evolution under visible light, ChemSusChem 10 (2017) 4624–4631.

[63] H. Li, Z. Liang, Q. Deng, M.T. Hu, N. Du, W. Hou, Facile construction of defect-rich rhenium disulfide/graphite carbon nitride heterojunction via electrostatic assembly for fast charge separation and photoactivity enhancement, ChemCatChem 11 (2019) 1633–1642.

[64] M.A. Mohamed, M.F.M. Zain, L. Jeffery Minggu, M.B. Kassim, J. Jaafar, N. A. Saidina Amin, M.S. Mastuli, H. Wu, R.J. Wong, Y.H. Ng, Bio-inspired hierarchical hetero-architectures of in-situ C-doped g-C3N4 grafted on C, N co-doped ZnO micro-flowers with booming solar photocatalytic activity, J. Ind. Eng. Chem. 77 (2019) 393–407.

[65] Z. Kou, T. Wang, Q. Gu, M. Xiong, L. Zheng, X. Li, Z. Pan, H. Chen, F. Verpoort, A. K. Cheetham, S. Mu, J. Wang, Rational design of holey 2D nonlayered transition metal carbide/nitride heterostructure nanosheets for highly efficient water oxidation, Adv. Energy Mater. 9 (16) (2019) 1803768, https://doi.org/10.1002/aenm.v9.1610.1002/aenm.201803768.

[66] J. Li, Y. Li, G. Zhang, H. Huang, X. Wu, One-dimensional/two-dimensional core-shell-structured Bi2O4/BiO2-x heterojunction for highly efficient broad spectrum light-driven photocatalysis: faster interfacial charge transfer and enhanced molecular oxygen activation mechanism, ACS Appl. Mater. Interfaces 11 (2019) 7112–7122.

[67] Y.-J. Yuan, Z. Shen, S. Wu, Y. Su, L. Pei, Z. Ji, M. Ding, W. Bai, Y. Chen, Z.-T. Yu, Z. Zou, Liquid exfoliation of g-C3N4 nanosheets to construct 2D–2D MoS2/g-C3N4 photocatalyst for enhanced photocatalytic H2 production activity, Appl. Catal. B, Environ. 246 (2019) 120–128.

[68] P. Karaolia, I. Michael-Kordatou, E. Hapeshi, C. Drosou, Y. Bertakis, D. Christofilos, G.S. Armatas, L. Sygellou, T. Schwartz, N.P. Xekoukoulotakis, D. Fatta-Kassinos, Removal of antibiotics, antibiotic-resistant bacteria and their associated genes by graphene-based TiO2 composite photocatalysts under solar radiation in urban wastewaters, Appl. Catal. B, Environ. 224 (2018) 810–824.

[69] K. Li, Z. Zeng, L. Yan, M. Huo, Y. Guo, S. Luo, X. Luo, Fabrication of C/X-TiO2@C3N4 NTs (X=N, F, Cl) composites by using phenolic organic pollutants as raw materials and their visible-light photocatalytic performance in different photocatalytic systems, Appl. Catal. B, Environ. 187 (2016) 269–280.

[70] J.-C. Wang, C.-X. Cui, Y. Li, L. Liu, Y.-P. Zhang, W. Shi, Porous Mn doped g-C3N4 photocatalysts for enhanced synergetic degradation under visible-light illumination, J. Hazard. Mater. 339 (2017) 43–53.

[71] Y. Deng, L. Tang, G. Zeng, J. Wang, Y. Zhou, J. Wang, J. Tang, L. Wang, C. Feng, Facile fabrication of mediator-free Z-scheme photocatalyst of phosphorous-doped ultrathin graphitic carbon nitride nanosheets and bismuth vanadate composites with enhanced tetracycline degradation under visible light, J. Colloid. Interface Sci. 509 (2018) 219–234.

[72] Z. Chen, P. Sun, B. Fan, Q. Liu, Z. Zhang, X. Fang, Textural and electronic structure engineering of carbon nitride via doping with pi-deficient aromatic pyridine ring for improving photocatalytic activity, Appl. Catal. B, Environ. 170 (2015) 10–16.

[73] Q. Liang, X. Liu, G. Zeng, Z. Liu, L. Tang, B. Shao, Z. Zeng, W. Zhang, Y. Liu, M. Cheng, W. Tang, S. Gong, Surfactant-assisted synthesis of photocatalysts: mechanism, synthesis, recent advances and environmental application, Chem. Eng. J. 372 (2019) 429–451.

[74] W.K. Jo, S. Tonda, Novel CoAl-LDH/g-C3N4/RGO ternary heterojunction with notable 2D/2D/2D configuration for highly efficient visible-light-induced photocatalytic elimination of dye and antibiotic pollutants, J. Hazard. Mater. 368 (2019) 778–787.

[75] M. Ge, L. Liu, W. Chen, Z. Zhou, Sunlight-driven degradation of Rhodamine B by peanut-shaped porous BiVO4 nanostructures in the H2O2-containing system, Crystengcomm 14 (2012) 1038–1044.

[76] Y. Xia, B. Cheng, J. Fan, J. Yu, G. Liu, Near-infrared absorbing 2D/3D ZnIn2S4/N-doped graphene photocatalyst for highly efficient CO2 capture and photocatalytic reduction, Sci. China Mater. 63 (2020) 552–565.